Final Report for Period: 09/2010 - 08/2011 **Submitted on:** 09/22/2011
Principal Investigator: Lackey, W. Jack . **Award ID:** 0403671
Organization: Georgia Tech Research Corp
Submitted By:
Lackey, W. Jack - Principal Investigator
Title:
NIRT: Electron Beam Chemical Vapor Deposition (CVD) - A New Tool for Manufacturing Nanomaterials and Devices

Project Participants

Senior Personnel

Name: Lackey, W. Jack
Worked for more than 160 Hours: Yes
Contribution to Project:
Principal Investigator and active in focused EB-CVD.

Name: Wang, Zhong
Worked for more than 160 Hours: Yes
Contribution to Project:
Co-PI for characterization.

Name: Fedorov, Andrei
Worked for more than 160 Hours: Yes
Contribution to Project:
Co-PI for focused beam EB-CVD and modeling.

Name: Orlando, Thomas
Worked for more than 160 Hours: Yes
Contribution to Project:
Co-PI for broad beam EB-CVD.

Name: Johnson, Ryan
Worked for more than 160 Hours: Yes
Contribution to Project:
Assisted in equipment set-up and statistical design and analysis of experiments.

Post-doc

Name: Ding, Yong
Worked for more than 160 Hours: Yes
Contribution to Project:
Performed SEM, TEM, EDS, and EELS on platinum and carbon deposits. Was the lead in this effort.

Graduate Student

Name: Shepperd, Kristen
Worked for more than 160 Hours: Yes
Contribution to Project:
Lead student in setting up the broad beam EB-CVD system and the conduct of experiments.

Name: Lane, Christopher
Worked for more than 160 Hours: Yes
Contribution to Project:
Assisted in conduct of broad beam EB-CVD experiments and lead student in modeling this process.

Name: White, Ben
Worked for more than 160 Hours: Yes
Contribution to Project:
Lead student in modeling the focused EB-CVD process and also conducted EB-CVD deposition experiments.

Name: Mi, Jian
Worked for more than 160 Hours: Yes
Contribution to Project:
Assisted in deposit characterization.

Name: Bondi, Scott
Worked for more than 160 Hours: Yes
Contribution to Project:
Minor role in modification of the EB-CVD syatem and teaching of other students about SEM.

Name: Kim, S.
Worked for more than 160 Hours: Yes
Contribution to Project:

Name: Henry, M.
Worked for more than 160 Hours: Yes
Contribution to Project:

Undergraduate Student

Name: Wiley, Shek
Worked for more than 160 Hours: Yes
Contribution to Project:
Assisted in characterization of deposits.

Name: Rykaczewski, Konrad
Worked for more than 160 Hours: Yes
Contribution to Project:
Assisted Ben White in modeling and experimentation as an undergraduate student and now as a graduate student conducts focused beam EB-CVD experiments and models the process.

Name: Browning, Jenna
Worked for more than 160 Hours: Yes
Contribution to Project:
Assisted grad students in all phases (equipment specification and set-up, EB-CVD experimentation, and modeling) of this research project.

Name: Marshall, Andrew
Worked for more than 160 Hours: Yes
Contribution to Project:
Assisted grad students in all phases (equipment specification and set-up, EB-CVD experimentation, and modeling) of this research project.

Name: Pi, D.
Worked for more than 160 Hours: Yes
Contribution to Project:

Technician, Programmer

Other Participant

Research Experience for Undergraduates

Organizational Partners

FEI Inc.

Several members of the FEI, Inc. staff have made important contributions to this research. This includes maintenance of the ESEM without cost, design of a generic gas injection system, and advice on deposition of platinum. FEI,Inc. has made these contributions since they view our research as furthering the science and technology of EB-CVD which they feel will promote sale of EB-CVD systems.

Other Collaborators or Contacts

Professor Ian Ferguson of Georgia Tech's School of Electrical and Computer Engineering, on potential use of FEB-CVD to grow nanostructures for spintronics applications.
IBM and Global Foundries, Inc. on making metal-carbon nanotube/graphene interconnects.

Activities and Findings

Research and Education Activities: (See PDF version submitted by PI at the end of the report)

Introduction

Nanoscale materials and devices offer great promise for many important civilian and military applications, but their fabrication often proves problematic. Similarly, integrating nanostructures with microsystems or other nano structures is one of the main roadblocks to transitioning from single structure fabrication to true nanomanufacturing. This research focuses on a technology that has an excellent potential for solving these problems. It is Electron Beam Chemical Vapor Deposition or simply EB-CVD. Specifically, two electron beam processes are being developed. Both are capable of depositing metals and ceramics by EB-CVD and are complimentary in nature. The first process uses a tightly focused electron beam, i.e., beam diameters as small as 1 nm, to achieve high spatial resolution of the fabricated structures. The second process uses a broad beam and relies on constructive and destructive interference to permit patterning of large areas, leading to high throughput manufacturing. The judicious combination of these two processes offers a unique opportunity to manufacture very complex structures by computer-controlled concurrent movement of the narrowly focused and broad beams relative to the substrate.

The goals of this NIRT research project were:

1) To develop a novel nanoscale manufacturing tool that utilizes EB-CVD, electron beam surface enhancement, or etching.
2) To obtain a fundamental understanding, via modeling and experimentation, of the physical, chemical, and materials phenomena that control deposition, surface enhancement, and etching.
3) To identify process-nanostructure-property relationships for a key set of materials that will permit fabrication of advanced nanoscale materials and devices, including integrating nanomaterials with microsystems.

An electron beam has been shown to interact with reagent

chemicals that are adsorbed onto the surface of a solid substrate causing a chemical reaction(s) that leads to the deposition of a solid metal or ceramic onto the substrate. Importantly, the deposition occurs with minimal heating and thus sensitive substrates or previous deposits are not thermally damaged. Since electron beams can be focused to spot sizes on the order of 1 nm, it is possible to fabricate truly nanoscale devices. Our research will permit establishing the scientific and engineering knowledge base necessary to permit efficient use of EB-CVD for fabrication of nanoscale materials and devices. By automating beam movement with a commercially available beam patterning system, it will be possible to rapidly and reproducibly fabricate truly nanoscale materials and devices of 2-D and 3-D architecture and to use the system to integrate nanomaterials with microsystems.
Results for the EB-CVD processes being studied as well as modeling of these processes appear in the attached file.

Findings: (See PDF version submitted by PI at the end of the report)

Our advances in fundamental understanding of the EBID process, as described in the previous attachment, have been applied to development of two new nanomanufacturing processes relevant to important applications: (1) making a low-temperature Ohmic contact for the next generation of electric interconnects based on ballistically-conducting multiwalled carbon nanotubes (MWCNTs) and (2) resist-free rapid prototyping of high-aspect-ratio, topologically-complex three-dimensional (3D) metal-semiconductor nanostructures using electron beam assisted deposition of amorphous carbon in combination with metal assisted chemical etching (EBID-MaCE). The results demonstrated have been well received by the technical community and are currently being expanded to other applications.

Specific conclusions follow:
? Mass transport to the growing deposit determines the overall growth rate of the deposit.

? The mass transport to the deposit is both diffusive (far from the deposition zone) and ballistic (near the deposit) in nature.

? Secondary electron scattering within the substrate and deposit determines the morphology of the deposit. The deposit shape can be controlled by changing the characteristics of the primary electron beam as well as the properties of the substrate.

? Electron scattering by the precursor gas in the deposition chamber can significantly hinder the growth of the deposit at high (> 5 torr) chamber pressures. To address this challenge, the micro-needle gas injection system was developed for precise delivery of the precursor to the deposition spot in minute quantities

? High resolution transmission electron microscope images of platinum deposits have revealed mainly amorphous structure with presence of nanocrystals. The crystallinity of the deposits was shown to increase by annealing at elevated temperatures.

? Depositing carbon using methane as a precursor has been optimized to achieve a repeatable process by careful control of the deposition conditions.

? Carbon was successfully deposited using acetylene as a precursor. This was the first ever demonstration of such a process.

? Silicon carbide nanostructures were successfully deposited using monomethylsilane as a precursor.

Training and Development:

Importantly, numerous students participated in actual device fabrication. The graduate and undergraduate students working on the project have become proficient in the use of NPGS software for control of the electron microscope for EB-CVD. This understanding of the fundamental principles and practical aspects of operation of the electron microscope has also been supported by course work on the theory of electron microscopy. Importantly, the undergraduate students have gotten to see how research is planned, conducted, and analyzed.

There are three Ph.D. students intimately involved in this project who are making EB-CVD their thesis topic. As the theoretical side of this project is being advanced by the development of process models, emphasis is also being placed on training and practice with the focused and broad beam EB-CVD systems. Thus, these students are learning about equipment, experimentation, and modeling. Through familiarization with the equipment and procedures used in the process it will be possible to validate the model results through experimentation.

All three graduate students are also intimately concerned with understanding the fundamental chemistry and physics involved in electron-beam enhanced chemical vapor deposition, electron-surface and electron molecule scattering. There is close coupling to the experimental and modeling and theory efforts underway in the laboratories involved. Frequent meetings prompt exchange of progress and ideas between the four professors and students involved in this interdisciplinary research.
Two undergraduate students, enrolled in the mechanical engineering program here at Georgia Tech, previously participated in the NIRT research activities as NSF REU fellows. They were fully trained on the operation of the scanning electron microscope and all supporting equipment, and have performed a number of independent deposition experiments with the EB-CVD system. They were also actively engaged in the critical analysis of the available EB-CVD literature as well as development of the EB-CVD models. They report very positive experiences.

All of the undergraduate and graduate students have the opportunity to see how a large interdisciplinary research project is conducted/managed via our group meetings and presentations.

One post-doc student is also active on the project. He is responsible

for deposit characterization and teaching both undergraduate and graduate students the science and art of SEM/TEM/EDS/EELS.

Demonstrations on molecules, color, and temperature to the Morris Brandon Elementary School 1st and 2nd Grades were performed.

The science and technology of EB-CVD was introduced in at least two graduate level courses.

Outreach Activities:

Dr. Orlando made presentations to Kindergarten and 1st grade students at the Morris Brandon Elementary School, Atlanta Public School on molecules, color, and temperature.
Dr. Lackey mentored an elementary student.
Dr. Wang made a number of presentations to the general public, at universities, and at international conferences on nanoscience. Prof. Fedorov and his students' research in FEB-CVD was featured in a documentary by the Bavarian educational TV network 'Global Engineering Education-U.S. Perspective' (filmed in April 2007, and released in September 2007).

Journal Publications

David C. Beaulieu, Yong Ding, Z. L. Wang, and W. J. Lackey, "Influence of process variables on electron beam chemical vapor deposition of platinum", J. Vacuum Science and Technology B, p. 126, vol. Sept, (2005). Published,

David Beaulieu and W. Jack Lackey, "Electron Beam Chemical Vapor Deposition: Materials, Modeling, and Applications", International Material Reviews, p. 112, vol. , (2005). Published,

Christopher D. Lane, Kristin R. Shepperd, Alex B. Aleksandrov, and Thomas M. Orlando, "Electron stimulated desorption of cations from SiCl4 multilayers adsorbed on Si(111", Surface Science, p. 173, vol. 593, (2005). Published,

T. M. Orlando, "Nanopatterning of 3-D Structures using Quantum Interference Effects in Electron-stimulated Desorption", Materials Research Society, p. , vol. , (2004). Submitted,

Christopher D. Lane, Kristin R. Shepperd, Alex B. Aleksandrov, and Thomas M. Orlando, "Electron stimulated desorption of cations from SiCl4 multilayers adsorbed on Si(111)", 11th International Conference on Desorption Induced by Electronic Transitions (DIET 11) Susono, Japan, p. , vol. , (2004). Accepted,

K. Rykaczewski, B. White, J. Browning, A. D. Marshall, A. Fedorov, "A Dynamic Model of Electron Beam Induced Deposition (EBID) of Residual, Hydrocarbons in electron Microscopy, , Chicago, IL, November5-10, 2006.", International Mechanical Engineering Congress and Exposition IMECE'06, p. , vol. Nov., (2006). Submitted,

B. white, W. Lackey, and A. Fedorov, "Scaling and Limiting Case Models for Electron Beam Chemical Vapor Deposition (EBCVD)", International Mechanical Engineering Congress and Exposition IMECE'06, p. , vol. Nov., (2006). Submitted,

Christopher D. Lane and Thomas M. Orlando, "Low-energy electron-stimulated desorption of neutrals from multilayers of SiCl4 on Si(111)", Journal of Chemical Physics, p. 164702-1, vol. 124, (2006). Accepted,

Christopher D. Lane, "Inelastic electron scattering and energy-selective negative ion reactions on surfaces and interfaces", Applied Surface Science, p. , vol. , (2006). Submitted,

C. D. Lane and T. Orlando, "Electron-stimulated desorption from SiCl4 layers: Detection of cationic and neutral products", 231st National Am. Chem. Soc. Meeting, symposium on Theoretical and Experimental Advances in the Study of Low-Energy Electron-Induced Processes, p. , vol. March, (2006). Submitted,

W.B. White, K. Rykaczewski, and A. Fedorov, "What Controls Deposition Rate in Electron Beam Chemical Vapor Deposition?", Phys. Rev. Lett., p. 086101, vol. 97, (2006). Published,

K. Rykaczewski, W. B. White, and A Fedorov, "Analysis of Electron Beam Induced Deposition (EBID) of Residual Hydrocarbond in Electron Microscopy", J. appl. Phys. A, p. 054307, vol. 101, (2007). Published,

A Fedorov, K. Rykaczewski, and W. White, "Transport Issues in Focused Electron Beam Chemical Vapor Deposition", Surface and Coatings Tech., p. , vol. , ( ). Accepted,

Rykaczewski, K., Marshall, A., White, W.B., and Fedorov, A., "Dynamic growth of carbon nanopillars and nanorings in electron beam induced dissociation of residual hydrocarbons", Ultramicroscopy, p. , vol. , (2008). Accepted,

Fedorov, A., Rykaczewski, K., and White,W., "Transport issues in focused electron beam chemical vapor deposition", Surface & Coatings Technologies, p. 8808, vol. 201, (2007). Published,

Yang, Rusen; Qin, Yong; Li,Cheng; Zhu,Guang;Wang, Zhong Lin, "Converting Biomechanical Energy into Electricity by a Muscle-Movement-Driven Nanogenerator", Nano Letters, p. 1201, vol. 9, (2009). Published,

Konrad Rykaczewski, Owen J. Hildreth, Dhaval Kulkarni, Matthew R. Henry, Song-Kil Kim, Ching Ping Wong, Vladimir V. Tsukruk, and Andrei Federov, "Maskless and Resist-Free Rapid Protyping of t-Dimensional Structures Through Electron Beam Induced Deposition (EBID) of Carbon in Combination with Metal-Assisted Chemical Etching (MaCE) of Silicon", ACS Applied Material Interfaces, p. 969, vol. 2, (2010). Published,

Konrad Rykaczewski, Matthew R Henry, Song-Kil Kim, Andrei G Fedorov, Dhaval Kulkarni, Srikanth Singamaneni and Vladimir V Tsukruk, "The effect of the geometry and material properties of a carbon joint produced by electron beam induced deposition on the electrical resistance of a multiwalled carbon nanotube-to-metal contact interface", Nanotechnology, p. 035202, vol. 21, (2010). Published,

??? Rykaczewski, K., Henry, M., and Fedorov, "Electron beam induced deposition of residual hydrocarbons in the presence of a multiwall carbon nanotube", Appl. Phys. Lett, p. 113112, vol. 95, (2009). Published, 2009

??? Dietz, C., Rykaczewski, K., Fedorov, A. G., and Joshi, Y, "Visualization of droplet departure on a superhydrophobic surface and implications to heat transfer enhancement during drop-wise condensation", Appl. Phys. Lett, p. 033104, vol. 97 (3), (2010). Published,

??? Rykaczewski, K., Hildreth, O.J., Kulkarni, D., Henry, M., Kim, S-K., Wong, C.P., Tsukruk, V. V., and Fedorov, A, "Maskless and resist-free rapid prototyping of three dimensional silicon structures through Electron Beam Induced Deposition (EBID) of carbon in combination with Metal assisted Chemical Etching (MaCE) of Silicon", ACS Appl. Mat. & Interfaces, p. 969, vol. 2 (4), (2010). Published, 2010

??? Rykaczewski, K., Hildreth, O.J., Wong, C.P., Fedorov, A., and Scott, J. H. J, "Directed 2D-to-3D pattern transfer method for controlled fabrication of topologically complex three-dimensional features in silicon", Adv. Mater., p. 659, vol. 23 (5), (2011). Published, 2011

??? Henry, M. R., Kim, S., Rykaczewski, and Fedorov, "Inert gas jets for growth control in electron beam induced deposition", Appl. Phys. Lett, p. 263109, vol. , (2011). Published, 2011

?????? Rykaczewski, K., Hildreth, O.J., Wong, C.P., Fedorov, A., and Scott, J. H. J, "Guided three-dimensional catalyst folding during Metal-assisted Chemical Etching of silicon", Nano Lett., p. 2369, vol. 11 (6), (2011). Published, 2011

Books or Other One-time Publications

? Rykaczewski, K., White,
B., Browning, J., Marshall, A.
D. and Fedorov, A, "Dynamic model of electron beam
induced deposition (EBID) of
residual hydrocarbons in
electron microscopy", (2006). Conference, Published
Bibliography: International Mechanical
Engineering Congress &
Exposition IMECE'06, Chicago, IL

? Sun, L., White, W. B.,
Rykaczewski, Wingkono, G. A.,
Fedorov, A., and T. M. Orlando, "Focused electron beam chemical
vapor deposition of a periodic
silicon carbine nano-pattern", (2006). Book, Published
Bibliography: Materials Research Society
(MRS) Fall 2006 Meeting,
Boston, Massachusetts,
November 28-30.

? Rykaczewski, K., and
Fedorov, A, "Electron beam induced
deposition (EBID) of carbon
interface between a carbon
nanotube interconnect and
metal electrode", (2009). Conference, Published
Bibliography: Materials Research Society
(MRS) Spring 2009 Meeting, San
Francisco, California, April
13-17

Dietz, C., Rykaczewski,
K., Fedorov, A., and Joshi,Y., "ESEM imaging of condensation on
a nanostructured,
superhydrophobic surface", (2009). Conference, Published
Bibliography: International Mechanical
Engineering Congress and
Exposition (IMECE-2009), Lake
Buena Vista, Florida, November
13-19

? Kulkarni, D.,
Singamaneni, S., Tsukruk, V.V.,
Rykaczewski, K., and Fedorov, A, "Physical properties of
Electron beam induced
deposited (EBID) carbon -
Multiwalled carbon nanotube
(MWNT) - metal interface", (2010). Conference, Published
Bibliography: Materials Research Society (MRS)
Spring 2010 Meeting, San
Francisco, California, April 5-9

? Rykaczewski, K.,
Hildreth, O.J., Wang, C. P.,
Fedorov, A., Scott, J. H. J.,

and Maslar, J. E, "Maskless and Resist-Free Rapid Prototyping of Integrated Insulator, Semiconductor, and Conductor Three Dimensional Structures with Rotational Geometry through Electron Beam Induced Deposition (EBID) of Carbon and Focused Ion Beam ...", (2010). Conference, Published Bibliography: Materials Research Society (MRS) Fall 2010 Meeting, Boston, Massachusetts, November 29-December 3

? Rykaczewski, K., Hildreth, O.J., Wong, C.P., Fedorov, A., and Scott, J. H. J, "3D silicon nanostructures fabrication via thin film focused ion beam milling in combination with metal assisted chemical etchin", (2011). Conference, Published Bibliography: Materials Research Society (MRS) Spring 2011 Meeting, San Francisco, California, April 25-29

Web/Internet Site

Other Specific Products

Contributions

Contributions within Discipline:

Our work contributes directly and on the most fundamental level to a number of disciplines, including manufacturing sciences (CVD), heat, mass, and electron transport, electron microscopy, and surfaces sciences. This includes uncovering new facts about fundamental behavior of materials and electron-matter interactions on the nanoscale through experimental work, as well as development of basic understanding and means for process control by theoretical analysis and mathematical modeling of the complex and highly interacting physico-chemical processes underlying EB-CVD and occurring on a multitude of length and time scales.

We have demonstrated that the chamber scale precursor transport is the rate limiting step determining the growth rate of deposits in FEB-CVD.

We have demonstrated that the surface diffusion of adsorbed precursor molecules defines the shape of the deposit upon interaction with the secondary and back-scattered primary electrons.

We have identified the cascade of energy transfer from the impinging primary electrons to substrate/deposit electrons and phonons, and

under what conditions this would result in non-equilibrium heating of the deposit leading to change in its crystallinity.

The EB-CVD process offers great potential for the economical fabrication of nanoscale materials and devices. For this potential to be realized, the science and technology of EB-CVD must be advanced. This year we have made great progress toward that end goal. The growth of platinum and carbon dots, fibers, and lines has been shown to be very rapid and controllable. Extensive experimentation has established quantitative relationships between the key process variables (voltage, current, spot size, and dwell time) and deposit characteristics (deposition rate, shape, aspect ratio, uniformity, and structure). This information provides insight into the deposition mechanism as well as provides processing maps that will be very useful for manufacturers of nanoscale devices.

Graduate and undergraduate students from the School of Chemistry and Biochemistry, the School of Mechanical Engineering, and the School of Materials Science and Engineering are receiving valuable interdisciplinary training in Physical Chemistry, Materials Science, and Physics. The overall program emphasis is to develop a fundamental understanding of electron beam enhanced CVD of nanostructures so that a scaleable processing technology can be developed. Thus, the training is truly mixed between fundamental science and applied engineering.

Contributions to Other Disciplines:

We demonstrated a resist-free rapid prototyping method for fabricating three-dimensional structures using electron beam induced deposition. Our successful fabrication of a device that incorporates a multi-wall carbon nanotube demonstrates the utility of the EB-CVD process. Our understanding of platinum deposition will be of direct benefit to a broad array of manufacturers of microelectronics. Both manufacture and repair of micro and nano scale devices will be of immense industrial value.

The knowledge of electron-adsorbate interactions gained from this research project has broad applicability to many other disciplines, for example, hydrogen generation. As the project matures, we will greatly advance the science in this important area of chemical physics.

We have developed a general theoretical methodology and identified the dimensionless criteria that define transition from transport-limited to reaction-limited growth of nanostructures.

We have developed a scaling theory supported by experiments, which permits evaluation of energy dissipation cascade in electron beam mediated materials processing and electron microscopy.

As a part of the commitment to the Multiscale Integrated hermofluidic

research group within the Mechanical Engineering Department, a seminar was given to other graduate students within the department. This seminar covered a basic overview of the EB-CVD project and the modeling work done to date. In addition to serving informative purposes, it also allowed valuable, critical feedback on the project from students working in a variety of areas.

Contributions to Human Resource Development:

The project has been of direct value to numerous graduate and undergraduate students. They have learned how to plan, conduct , analyze, and report scientific and technical information. Most of them have obtained experience in both experimentation and modeling. They have also gained experience through presentations and scientific/management meetings. They have also been exposed regularly to other disciplines, given the interdisciplinary nature of this project. Our contact with K-12 students hopefully will have an impact in the future.

Contributions to Resources for Research and Education:

The state-of-the-art EB-CVD system is a valuable research tool for Georgia Tech. We have on many occasions prepared samples of platinum deposits for other researchers at Georgia Tech who are not funded by this project but whose results (for example, electrical conductivity measurements) will benefit this project.
We have incorporated the science and technology of EB-CVD into several graduate courses at Georgia Tech.

Contributions Beyond Science and Engineering:

The knowledge gained by FEI,Inc. through their interaction with us should result in the development of improved EB-CVD systems that will be available commercially. Such systems will permit industry to manufacture improved microelectronic and medical products. We have an on-going relationship on using electron beam deposition of carbon for making metal-CNT/graphene interconnects with the IBM T. J. Watson Research Center and Global Foundries, Inc.

Conference Proceedings

Categories for which nothing is reported:

Any Web/Internet Site

Any Product

Any Conference

FEB-CVD is a process by which a tightly-focused, high-energy electron beam, usually that of an electron microscope, impinges on a substrate. Through interaction with the substrate, the high energy primary electrons produce low energy secondary electrons some of which escape the surface of the substrate where they dissociate an adsorbed precursor gas into both a solid deposit and gaseous by-products. As the deposit grows, the electron beam also begins to interact with the deposit itself. Figure 1 shows a general schematic of the FEB-CVD process where precursor molecules are transported to the substrate where they adsorb onto the surface. Three methods of precursor gas introduction are common: complete flooding of the reaction chamber with the precursor, flooding of a smaller reaction cell within the chamber and local injection of the gas using very a fine needle. Once on the surface, the molecules are free to redistribute by surface diffusion. When the adsorbed molecules encounter electrons that are of the appropriate energy (typically secondary electrons), the precursor molecules dissociate or react to form a deposit. The nature of the deposit is dependent on many process variables including beam energy, current and width, precursor chemistry, method of precursor introduction, substrate properties, among others. FEB-CVD has shown promise for nanoscale deposition - smaller than 10 nm deposited structures have been reported [1] made from a variety of materials [2, 3]. Potential applications of this process include one-step nanofabrication [4, 5], micro fabrication mask repair [6], integrated circuit fabrication, and fabrication of high resolution scanning tunneling [7] and atomic force microscope tips.

In an attempt to characterize the electron beam chemical vapor deposition process extensive experimentation has been performed under a wide variety of conditions and with many different precursors. However, limited advances have been made in providing theoretically sound and experimentally validated understanding of the basic underlying physics. Silvis-Cividjian et al. [8] used simulation techniques developed for electron microscopy (Monte Carlo simulations) to investigate the role of electron scattering and secondary electron production in the deposit profile evolution. This work was later extended by others [9, 10], but accurate predictions of the deposit growth rate (both qualitative, i.e., correct functional dependence on the system parameters, and quantitative, i.e., accurate magnitude of the growth rate) have been elusive. Furthermore, consideration of the precursor gas transport to the deposition zone, both bulk-to-surface and on the surface, has been ignored and theoretical work in this field has been limited to electron-solid interaction.

Chamber Scale Transport

To identify the growth limiting process, a comparison time scales for relevant physical phenomena can be made. For the precursor molecules, there is a time scale associated with their transport to the substrate τ_T, a time scale for adsorption onto the substrate τ_A, and a time scale on which the deposition reaction occurs τ_R. For the electrons, there is a time scale for transport from the electron source (i.e., the zone within the substrate where secondary electrons are generated) to the deposition zone τ_E. These time scales need to be compared to the observation time scale τ_O on which the growth of the deposit can be practically measured in experiments. It must be noted that to estimate the time scale for precursor transport, the type of transport (diffusive or ballistic) must be assumed. Here, we consider both since either the local (deposit scale) or global (chamber scale) transport may dominate depending on the deposition mode. Using typical system parameters and precursor(CH_4)/substrate(Si) properties all relevant time scales can be estimated ($\tau_{T-diffusive} \sim 10^{-1}$ s, $\tau_{T-ballistic} \sim 10^{-4}$ s [11], $\tau_A \sim 10^{-6}$ s, $\tau_R \sim 10^{-5}$ s, $\tau_E \sim 10^{-9}$ s, $\tau_O \sim 10^{2}$ s). Since τ_T is the largest process time scale the precursor transport is the slowest and, therefore, the rate limiting process; and

all processes, including precursor transport, can be treated as quasi-steady-state with respect to the much greater observation time scale.

With this understanding, we consider four simple scaling models that could predict the trends associated with transport-limited deposit growth in FEB-CVD [12]. These models result from application of mass conservation by equating the deposition rate to the rate of precursor mass transfer to deposit. Specifically, we consider two stages of deposition: early hemispherical growth upon nucleation and longer-term growth of a cylindrically-shaped deposit with limited lateral broadening. Such experimentally observed deposit shapes are defined by the location of the primary electron scattering, i.e., within an unbounded substrate (hemispherical growth) vs. within the confines of the deposit itself (cylindrical growth). Using the gas kinetic theory, it is predicted that in the case of ballistic precursor transport to the hemispherical deposit, the deposit radius increases linearly with time $r \sim t$ (model 1). For ballistic transport to the top of a cylindrical deposit (treated as a hemispherical cap), the deposit radius is constant and its characteristic size (height h) still grows linearly with time $h \sim t$ (model 2). If the continuous (chamber scale) diffusive transport is rate limiting, the early (hemispherical) and longer-term (cylindrical) growth of the deposit should follow the relationships $r \sim t^{1/2}$ (model 3) and $h \sim t$ (model 4), respectively. It is important to note that all models except for continuous diffusion to a hemispherical deposit (model 3) predict a linear dependence of the deposit size on time. Additionally, when diffusive transport is assumed, the models predict that the overall size of the deposit will be independent of the pressure.

To determine which of the scaling relationships and associated transport modes govern FEB-CVD we have performed a set of carefully controlled experiments [12]. A 10% methane (precursor) 90% argon precursor was used to deposit carbon onto a polished silicon substrate. Deposits obtained for an electron beam energy of 25 keV, a beam current of 1100 pA, and for a working distance (between the electron column and substrate) of 10.5 mm can be seen in Figure 2 (a). These deposits are fairly cylindrical in shape and have a high aspect ratio. The height of these deposits as a function of time is shown in Figure 2(b). More hemispherical deposits were made using similar primary beam energy of 30 keV but a higher beam current of 5000 pA and are shown in Figure 3. The growth of the 25 keV cylindrical deposits (Fig. 2) and the 30 keV hemispherical deposits (Fig. 3) exhibit the approximately linear (model 4) and square-root (model 3) time dependences, respectively. This indicates that the rate-limiting step of FEB-CVD is continuous (chamber-scale) diffusion of precursor molecules to the deposition zone. Even though the deposit sizes in Fig. 3 are smaller overall than those in Fig. 2, the volume of the deposits is approximately the same (for a given deposition time and pressure). Thus the effect of an increase in beam current from 1100pA to 5000pA on the amount of material deposited is minimal.

Recall that the diffusive transport models predict no dependence of deposit growth rate on pressure. However, this behavior is not observed in Figs. 2 and 3. In reality, the size of the deposit decreases with an increase in the chamber pressure. This rules out the possibility of the ballistic precursor transport since it calls for an increase of the deposit size with pressure (models 1 and 2). If one considers how pressure affects the primary electron beam current actually reaching the substrate these results are not surprising. As the electrons pass through the gas-filled chamber they are scattered. The extent of scattering is dependent on the chamber pressure, the electron scattering cross section of the gas, and the distance traveled by the electrons to reach the substrate. Because of the exponential dependence of the scattering on pressure, a significant decrease (orders of magnitude for higher chamber pressures) in the number of electrons reaching the substrate could be expected. This reduced primary current results in a reduced number of "reactive" secondary electrons generated and, in turn, a reduction of the deposit size as the pressure increases. This observation is consistent with

the results shown in Figs. 2 and 3. An exponential decay in the beam current can be readily recovered from the experimentally measured deposit volumes as function of the chamber pressure. It is difficult to estimate the amount of scattering quantitatively since accurate scattering cross sections for the electron energies used for FEB-CVD are not available. Instead, we explored the effect of electron scattering experimentally. The results can be seen in Figure 4 which shows deposits made using the same system settings as those in Fig. 3 except that the working distance was decreased from 10.5 mm to 5.5 mm. The reduction in the beam travel distance, and thus its scattering, leads to an overall increase in the size of the deposits. Additionally, the deposition curves for different pressures closer together. Consistent with the chamber-scale, diffusion-limited mode of deposition, the results now exhibit minimal pressure-dependence especially at lower chamber pressures.

Surface Transport

Potential importance of surface diffusion contribution to overall mass transport in FEB-CVD has been brought up by several authors [8, 14]. Analysis of electron beam induced deposition (EBID) of residual hydrocarbon contamination in electron microscopy allows for evaluation of surface diffusion influence on the growth rates and shape of FEB-CVD deposits. Contamination deposition is a common phenomenon in electron microscopy most often manifested through formation of thin carbon films during imaging. With appropriate control of the electron beam carbon dots and lines [15] as well as sophisticated three dimensional carbon nanostructures [16] have been deposited. Muller [17], Reimer and Wachter [18], and Amman et al. [15] have explored experimental and theoretical aspects of the contamination deposition process, all coming to conclusion that surface diffusion is the dominant species transport mode. Amman et al. [15] proposed a rudimentary species transport model combined with a simplistic electron scattering model. However, formulation used by Amman is inadequate as it did not take into account transient spatial distribution of the precursor concentration and dynamic surface evolution effects. In our work [13] we have developed a comprehensive dynamic model of EBID coupling surface mass transport, electron transport and scattering, and precursor species decomposition to predict the deposition of carbon nanostructures. The governing surface transport equation has been derived, generalized by nondimensionalization, and solved numerically. In the derivation of the STE it is assumed that desorption and adsorption reached equilibrium, the nanostructure is radially symmetric, surface concentration changes due to dilution are negligible, and that the surface properties of the substrate and deposit are the constant.

$$\frac{\partial C^*}{\partial t^*} = \frac{t_{obs}}{t_{\mathrm{diff}}}\left(\frac{1}{r^*}\frac{\partial}{\partial s^*} r^* \frac{\partial C^*}{\partial s^*}\right) - \frac{t_{obs}}{t_{\mathrm{sink}}} C^* \dot{Q}^* \qquad (1)$$

Here, the starred quantities are rescaled concentration C^*, time t^*, deposit radius r^* and arc length s^*, and mass sink (reaction) term $\dot{Q}^*$. The relevant time scales include diffusion time scale t_{diff} equal to diffusion length scale (~ full width at 50% of the electron beam) squared divided by the surface diffusion coefficient ($= d_b^2 / D$), the mass sink (reaction) time scale t_{sink} equal to the inverse mass sink (reaction) scale, given by the product of primary electron flux j_{PE} with the secondary electron yield per primary electron δ_{SE} and maximum dissociation cross section $\sigma_{\max}$ ($= 1/ j_{PE}\delta_{SE}\sigma_{\max}$), and the observation time scale t_{obs} on which growth of deposit occurs. Based on the relative magnitudes of the diffusion (t_{diff}) and reaction (t_{sink}) time scales three distinct growth regimes can be identified. In case $t_{\mathrm{diff}} ? t_{\mathrm{sink}}$ deposition reaction is much faster than the surface

diffusion, resulting in diffusion-limited growth regime. In case $t_{diff} = t_{sink}$ surface diffusion is much faster than the reaction, resulting in a reaction-limited growth regime. The most general mixed reaction-diffusion growth regime occurs when $t_{diff} : t_{sink}$. The three possible deposition regimes have been simulated by selecting sets of physical variables corresponding to appropriate relationship between the relevant time scales. Details of the Monte Carlo electron scattering and generation models, discretization of and solution algorithm to the STE applied in the simulation are described in detail in Rykaczewski et al. [13]. Primary electron beam settings corresponding physical operation of FEI Quanta 200 ESEM have been used (beam diameter d_b=40nm, current of ~100pA, and accelerating voltage of 30 keV). Acetalene adsorption on Si(100) was selected as a representative precursor-substrate pair due to its well studied nature [19].

The simulated evolution of the deposit for total time of ~2.1s for reaction-limited, mixed (diffusion-reaction), and diffusion-limited cases are shown in Figs. 5(a)-5(c), while the corresponding precursor concentration profiles (mixed and diffusion limited-cases only) are shown in Figs. 6(a)-6(b). A maximal average vertical growth rate of 9.7 nm/s was obtained in the case of the reaction-limited deposition. In the case of the mixed diffusion-reaction regime, a lower surface diffusion coefficient results in decrease in the precursor supply to the reaction zone, thereby decreasing the averaged vertical growth rate to ~3.7 nm/s. For the simulated time of 2 seconds, only a thin film was deposited in the case of the diffusion-limited regime. Quantititative comparison between theoretical and experimental investigations calls for highly detailed information surface transport and reaction properties of the specific precursor-substrate pair, which is difficult to find and obtain experimentally. However, the results of our growth rate simulations [13] appear to be in a close agreement with the experimental vertical growth rates (5.6-50 nm/s) obtained by Ueda and Yoshimura [16] for various substrates and primary electron beam energies (5-30 keV).

It is important to point out that the vertical growth rate can be misleading measure of the deposition rate since it depends on the deposit shape. A volumetric deposition rate is shape-independent and far more instructive as a measure of deposition rate. We have shown that as oppose to the simulated vertical growth rate, the simulated volumetric deposition rates agree well with the deposition rate trends expected from scaling analysis. Nanopillars deposited in different deposition regimes not only grow at different rates, but also have different shapes. As shown in Fig. 7, when deposition is limited by mass transport not only is the deposition rate slower but in addition much broader structures are formed. The broadening of the nanopillars due to primary electron scattering and secondary electron generation within the deposit [8] does not play a significant role in widening of the shape in the early deposition stages discussed here. The broadening due to electron scattering within deposit is independent of the mass transport and occurs at further stages of the growth when deposit size is comparable to the electron mean free path (~20 nm at 30 keV in carbon) [20].

Use of Inert Gas Jet

Recently, we discovered that an inert, precursor free, argon jet is used to control the rate of EBID [21]. We demonstrated that a change in the jet inlet temperature either increases surface diffusion to greatly enhance the deposition rate or depletes the surface precursor due to impact-stimulated desorption to minimize the deposition or completely clean the surface. We have decoupled plasma effects from jet impingement and experimentally demonstrated that the plasma is not substantially contributing to the enhanced surface mobility of an adsorbed precursor. Instead, the energy transfer in the course of gas jet impingement has the effect of raising the precursor temperature, which consistently describes all phenomena observed in experiments. Use of an inert gas jet for EBID growth modulation is expected to be applicable to different modes of the precursor introduction to the

substrate, albeit perhaps in a more complex fashion when both the precursor and an inert gas are co-jetted onto the surface. Since the jet has a local effect on the surface and allows for rapid changes in the precursor behavior, this technique will allow for new degrees of freedom for EBID in nanomanufacturing. Additionally, a high-energy inert jet may be applied to locally clean the surface, which is of relevance to high-resolution SEM imaging.

Thermal Issues

Substrate and deposit heating by electron beam (EB) during FEBCVD has been hypothesized to affect deposit composition and crystallinity and may also affect precursor transport to the deposition zone. No direct experimental measurements of temperature rise within FEBCVD deposits are available due to small characteristic length scales. Theoretical treatment of the subject has also been limited to a few simplistic models [22]. Randolph et al. [22] implemented the single-scattering electron interaction Monte Carlo model described in detail by Joy [20] to predict a heat generation term for the steady state heat diffusion equation, which was then solved numerically. However, the assumption of diffuse transport of the heat carriers is questionable if characteristic length (e.g., a characteristic dimension of nanodeposit) is comparable to the mean free path of the heat carriers, which is the case for FEB-CVD. In such case the heat carriers (conduction electrons in metals and phonons in dielectrics) have to be modeled as discrete particles with their transport described by Boltzmann Transport Equation (BTE). Development of such a transport model is difficult and has not yet been applied to the electron beam heating problem. In this work, a time scale analysis of relevant high energy electron interactions with target materials and heat carrier transport (both electrons and phonons) is used to estimate thermal perturbation introduced by electron beam. Copper is selected as a representative material since it is often used as a substrate in electron microscopy imaging and many of the deposited materials are metallic. In the course of scattering in metal primary electron looses most energy due to excitation of conduction, valence, and core electrons [23]. The Fast Secondary Electron (FSE) model [20] can be used to estimate a total Inelastic Mean Free Path (IMFP) for these excitation processes. The averaged (0<E<20 keV) IMFP for copper is ~8.4 nm while the related time scale is $\tau_{PECu} = 1.4 \cdot 10^{-16}\,\mathrm{s}$. The electron-phonon scattering mean free path and the scattering time can be obtained from the electric resistivity data. For high-purity copper the electron-phonon scattering time τ_{e_c-ph} equals $2.5 \cdot 10^{-14}\,\mathrm{s}$, while the mean free path λ_{e_c-ph} is 38 nm [24]. Ziman [25] estimates the free electron-free electron scattering time $\tau_{e_c-e_c} \sim 10^{-12}\,\mathrm{s}$, which results in a mean free path $\lambda_{e_c-e_c}$ of $\sim 1.5\,\mu\mathrm{m}$ (assuming Fermi velocity of $\sim 1.5 \cdot 10^{6}\,\mathrm{m/s}$ [24]). Calculation of the phonon relaxation time in metals is not trivial. The phonon mean free path in metals depends on phonon-phonon (U-processes), phonon-electron and phonon-defect scattering. However since the temperature of interest (T~300K) is close to the Debye temperature for copper ($\theta_D = 340\,\mathrm{K}$ [24]) the phonon-mean free path can be roughly estimated by neglecting the phonon-electron and phonon-defect contributions. This yields a phonon mean free path λ_{ph} of ~7 nm [25]. Dividing the phonon mean free path by the average phonon speed of 5000m/s [24] results in the characteristic time for phonon scattering $\tau_{ph} \sim 1.5 \cdot 10^{-12}\,\boldsymbol{s}$. Comparing all relevant time scales for a primary electron scattering results in:

$$\tau_{ph} \sim \tau_{e_c-e_c} \; ? \;\; \tau_{e_c-ph} \; ? \;\; \tau_{PECu} \qquad (2)$$

Based on these time scales the proper formulation of high energy electron heating of a metal will involve solution of both the electron and phonon transport equations. The two transport equations are coupled through the electron-phonon collision integral described by Vasko [26]. The electron transport equation should include an electron source term to account for the perturbation introduced by the excited core and valence electrons. The source time scale τ_s represents time between two primary electrons impinging on the substrate and can be easily computed by dividing the charge of an electron by the electron beam current *I*. The calculated source time scales for electron beam currents used by Utke et al. [27] in experiments evaluating the thermal effects of electron beam heating are given in Table 1.

Table 1. Electron Beam currents used by Utke et al. [27] and corresponding source time scales

Current, I (pA)	20	112	1.1×10^{3}	1×10^{4}	8.2×10^{4}	3×10^{6}
τ_s (s)	8×10^{-9}	1.43×10^{-9}	1.45×10^{-10}	1.6×10^{-11}	1.95×10^{-12}	5.3×10^{-14}

For electron beam currents up to ~1000 pA τ_s ? $\tau_{ph} \sim \tau_{e_c-e_c}$? τ_{e_c-ph} ? τ_{PECu}. In such case both the local electron and phonon distributions will barely be perturbed by a primary electron and will reach equilibrium before another primary electron enters the substrate. In turn, energy dissipated by an individual primary electron over its trajectory within the metal target can be neglected, resulting in negligible heating and temperature rise. With currents in the 10-1000 nA range the electron source term time scale will be on the same order of magnitude as the phonon relaxation time. In such case the electron beam will start introducing a slight perturbation to the phonon distribution while the electron distribution will reach equilibrium quickly. Thus, in experiments with beam currents in the 10-1000 nA range a moderate and spatially uniform heating and temperature rise can be expected. If electron beam current is greater than ~(1-10) μA the electron source term time scale will be of the order of magnitude of the electron-phonon collision time scale or shorter. Such high currents will result in significant perturbation of both the electron and phonon distributions. With both distributions in non-equilibrium a significant heating and increase in target temperature are expected.

Utke et al. [28] have recently shown that beam current can affect both the composition and crystalline structure of the deposits of cobalt from $Co_2(CO)_8$ grown using FEB-CVD. Figure 8 shows cross sections of three different sets of deposits made. Deposits made using the lowest current (20 pA) have the lowest cobalt content and no apparent crystalline structure. Deposits made at the highest current (82 nA) have a much higher percentage of cobalt and exhibit some structural organization. It has been hypothesized that at high deposit temperatures (>100 C) more $Co_4(CO)_{12}$ is converted to metallic cobalt which results in a more pure cobalt deposit. Higher temperatures could also provide the energy for rearrangement of the deposited cobalt into a more favorable crystalline structure. Experimental finding of Utke [27, 28] support theoretical time scale analysis predictions presented in this paper. Currents of ~(20-1000) pA correspond to limited heating and, therefore, low metallic cobalt concentration. Whereas the currents higher than ~100 nA result in significant heating and an increase in cobalt concentration as well as deposit crystallinity.

Applications

Our advances in fundamental understanding of the EBID process, as described in the previous sections, have been applied to development of two new nanomanufacturing processes relevant to important applications: (1) making a low-temperature Ohmic contact for the next generation of electric interconnects (Fig. 9) based on ballistically-conducting multiwalled carbon nanotubes

(MWCNTs) [29-31] and (2) resist-free rapid prototyping of high-aspect-ratio, topologically-complex three-dimensional (3D) metal-semiconductor nanostructures (Fig. 10) using electron beam assisted deposition of amorphous carbon in combination with metal assisted chemical etching (EBID-MaCE) [32-34]. The results demonstrated has been well received by the technical community and are currently further expanded to other applications.

References

1. Silvis-Cividjian, N., et al., *Direct fabrication of nanowires in an electron microscope.* Appl. Phys. Lett., 2003. **82**(20): p. 3514-16.
2. Hoyle, P.C., J.R.A. Cleaver, and H. Ahmed, *Electron beam induced deposition from W(CO)6 at 2 to 20 keV and its applications.* J. Vac. Sci. Technol. B, 1996. **14**(2): p. 662.
3. Beaulieu, D., et al., *Influence of process variables on electron beam chemical vapor deposition of platinum.* J. Vac. Sci. Technol. B, 2005. **23**(5): p. 2151-2159.
4. Ooi, T., et al. *3D nano wire-frame for handling and observing a single DNA fiber*. 2000. Miyazaki, Japan: IEEE.
5. Boggild, P., et al., *Fabrication and actuation of customized nanotweezers with a 25 nm gap.* Nanotechnology, 2001. **12**(3): p. 331-5.
6. Kohlmann-von Platen, K.T., et al., *Electron-beam induced tungsten deposition: growth rate enhancement and applications in microelectronics.* J. Vac. Sci. Technol. B, 1992. **10**(6): p. 2690-4.
7. Akama, Y., et al., *New scanning tunneling microscopy tip for measuring surface topography.* J. Vac. Sci. Technol. A, 1990. **8**(1): p. 429-33.
8. Silvis-Cividjian, N., et al., *The role of secondary electrons in electron-beam-induced-deposition spatial resolution.* Microelectronic Engineering, 2002. **61-62**: p. 693-9.
9. Bret, T., et al., *In situ control of the focused-electron-beam-induced deposition process.* Applied Physics Letters, 2003. **83**(19): p. 4005-7.
10. Mitsuishi, K., et al., *Dynamic profile calculation of deposition resolution by high-energy electrons in electron-beam-induced deposition.* Ultramicroscopy, 2005. **103**(1): p. 17-22.
11. Clarke, J.F. and M. McChesney, *The Dynamics of Real Gases*. 1964, Washington D.C.: Butterworth & Co. Ltd.
12. White, W.B., K. Rykaczewski, and A.G. Fedorov, *What controls deposition rate in electron-beam chemical vapor deposition?* Physical Review Letters, 2006. **97**(086101).
13. Rykaczewski, K., W.B. White, and A.G. Fedorov, *Analysis of Electron Beam Induced Deposition (EBID) of residual hydrocarbons in electron microscopy.* Journal of Applied Physics, 2007. **101**(4).
14. Fowlkes, J.D., S.J. Randolph, and P.D. Rack, *Growth and simulation of high-aspect ratio nanopillars by primary and secondary electron-induced deposition.* Journal of Vacuum Science & Technology B (Microelectronics and Nanometer Structures), 2005. **23**(6): p. 2825-2832.
15. Amman, M., et al., *Atomic force microscopy study of electron beam written contamination structures.* Journal of Vacuum Science & Technology B (Microelectronics and Nanometer Structures), 1995. **14**(1): p. 54-62.
16. Ueda, K. and M. Yoshimura, *Fabrication of nanofigures by focused electron beam-induced deposition.* Thin Solid Films, 2004(464-465): p. 331-334.

17. Muller, K., *Elektronen mikroschreiber mit geschwindigkeitsgesteuerter strahlfurung. II.* Optik, 1971. **33**: p. 296.
18. Reimer, L. and M. Wachter, *Contribution to the contamination problem in Transmission Electron Microscopy.* Ultramicroscopy, 1978. **3**: p. 169-174.
19. Taylor, P.A., et al., *Adsorption and Decomposition of Acetylene of Si(100)-(2x1).* Journal of American Chemical Society, 1992. **114**: p. 6754-6760.
20. Joy, D.C., *Monte Carlo Modeling for Electron Microscopy and Microanalysis*. 1995, New York, London: Oxford University Press.
21. Henry, M. R., Kim, S., Rykaczewski, and Fedorov, A., Inert gas jets for growth control in electron beam induced deposition, *Appl. Phys. Lett.,* **98**, 263109 (2011).
22. Randolph, S.J., J.D. Fowlkes, and P.D. Rack, *Effects of heat generation during electron-beam-induced deposition of nanostructures.* Journal of Applied Physics, 2005. **97**(12): p. 124312.
23. Dapor, M., *Electron-beam interactions with solids : application of the Monte Carlo method to electron scattering problems*. 2003, Berlin ; New York: Springer.
24. Zhang, Z., *Nano/microscale Heat Transfer*. 2007: McGraw-Hill.
25. Ziman, J.M., *Electrons and phonons; the theory of transport phenomena in solids*. The International series of monographs on physics. 1960, Oxford: Clarendon Press.
26. Vas'ko, F.T. and O.E. Raichev, *Quantum kinetic theory and applications : electrons, photons, phonons*. 2005, New York: Springer.
27. Utke, I., et al., *Thermal effects during focused electron beam induced deposition of nanocomposite magnetic-cobalt-containing tips.* Microelectronic Engineering, 2004. **73-74**: p. 553-8.
28. Utke, I., et al., *Cross section investigations of compositions and sub-structures of tips obtained by focused electron beam induced deposition.* Advanced Engineering Materials, 2005. **7**(5): p. 323-331.
29. Rykaczewski, K., M.R. Henry, and A.G. Fedorov, *Electron beam induced deposition of residual hydrocarbons in the presence of a multiwall carbon nanotube.* Applied Physics Letters, 2009. **95**(11), 113112.
30. Rykaczewski, K., M.R. Henry, S.K. Kim, A.G. Fedorov, D. Kulkarni, S. Singamaneni, and V.V. Tsukruk, *The effect of the geometry and material properties of a carbon joint produced by electron beam induced deposition on the electrical resistance of a multiwalled carbon nanotube-to-metal contact interface*. Nanotechnology, 2010. **21**(3), 12.
31 Kulkarni, D., Rykaczewski, K., Singamaneni, S., Kim, S-K., Fedorov, A., and Tsukruk, V. V., *Thermally-induced transformations of amorphous carbon nanostructures fabricated by Electron Beam Induced Deposition*, ACS Appl. Mat. & Interfaces, **3**(3), 710-720 (2011).
32. Rykaczewski, K., O.J. Hildreth, D. Kulkarni, M.R. Henry, S.K. Kim, C.P. Wong, V.V. Tsukruk, and A.G. Fedorov, *Maskless and resist-free rapid prototyping of three-dimensional structures through Electron Beam Induced Deposition (EBID) of carbon in combination with Metal-assisted Chemical Etching (MaCE) of silicon.* ACS J. Applied Materials and Interfaces. 2010, **2**(4), 969.
33. Rykaczewski, K., Hildreth, O.J., Wong, C.P., Fedorov, A., and Scott, J. H. J., *Directed 2D-to-3D pattern transfer method for controlled fabrication of topologically complex three-dimensional features in silicon,* Adv. Mater., **23(** 5), 659-663 (2011).

34. Rykaczewski, K., Hildreth, O.J., Wong, C.P., Fedorov, A., and Scott, J. H. J., Guided three-dimensional catalyst folding during Metal-assisted Chemical Etching of silicon, *Nano Lett.*, **11** (6), 2369-2374 (2011).

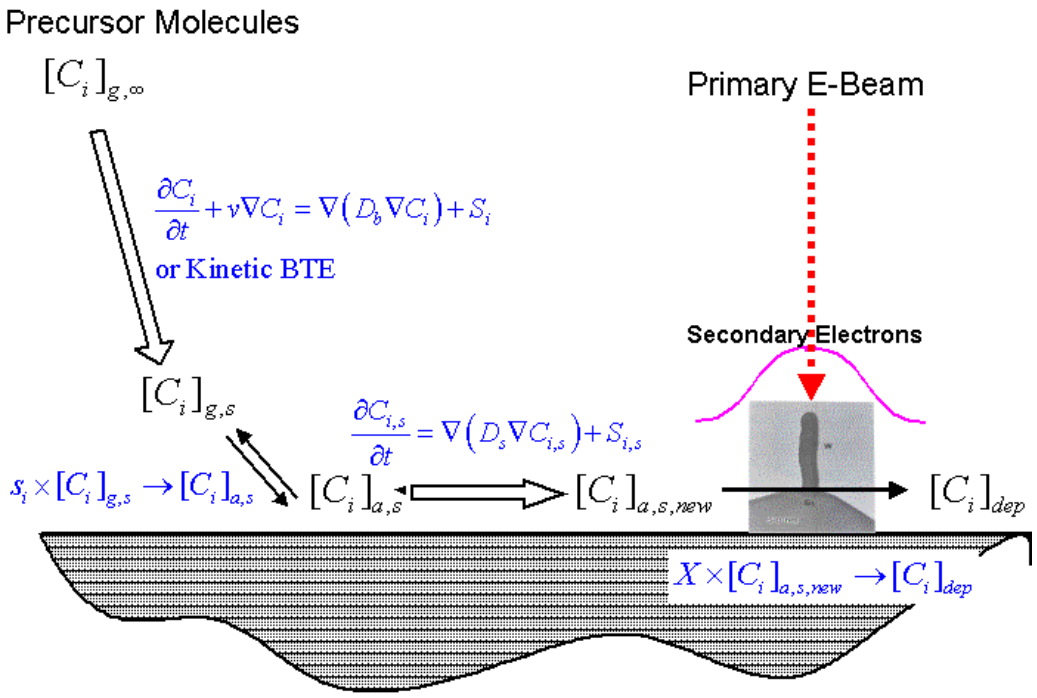

Figure 1: Schematic of Electron Beam deposition & key transport processes.

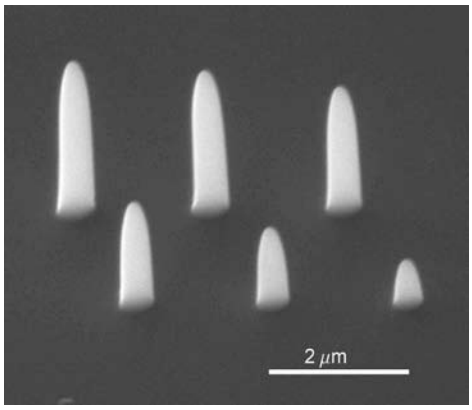

(a)

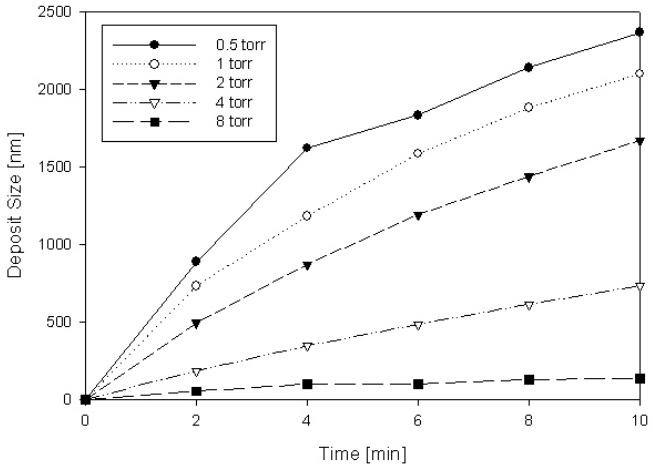

(b)

Figure 2: Carbon deposition with 25 keV, 1100 pA e-beam at 10.5 mm working distance: (a) SEM micrographs of the 1 torr deposits, (b) Deposit size as a function of time for various chamber pressures.

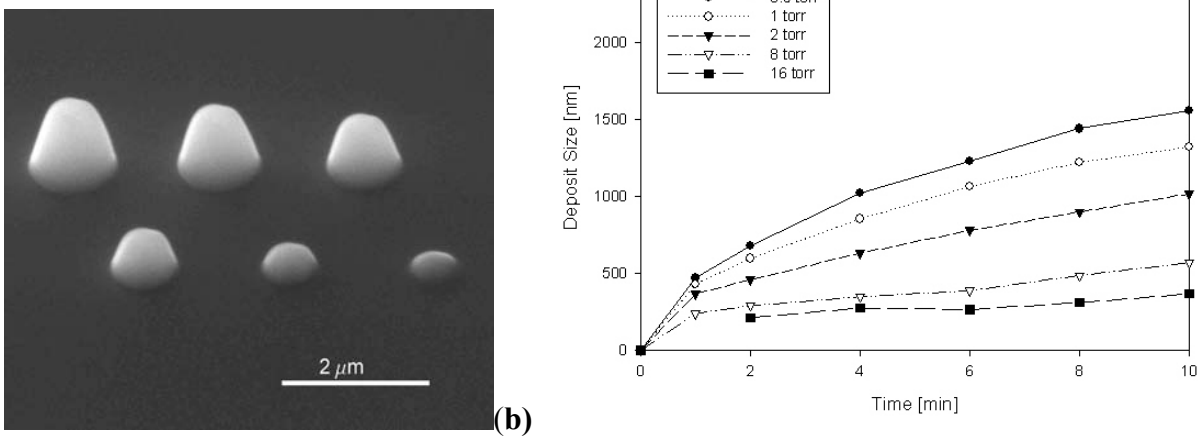

(a) **(b)**

Figure 3: Carbon deposition with 30 keV, 5000 pA e-beam at 10.5 mm working distance: (a) SEM micrographs of the 1 torr deposits, (b) Deposit size as a function of time for various chamber pressures.

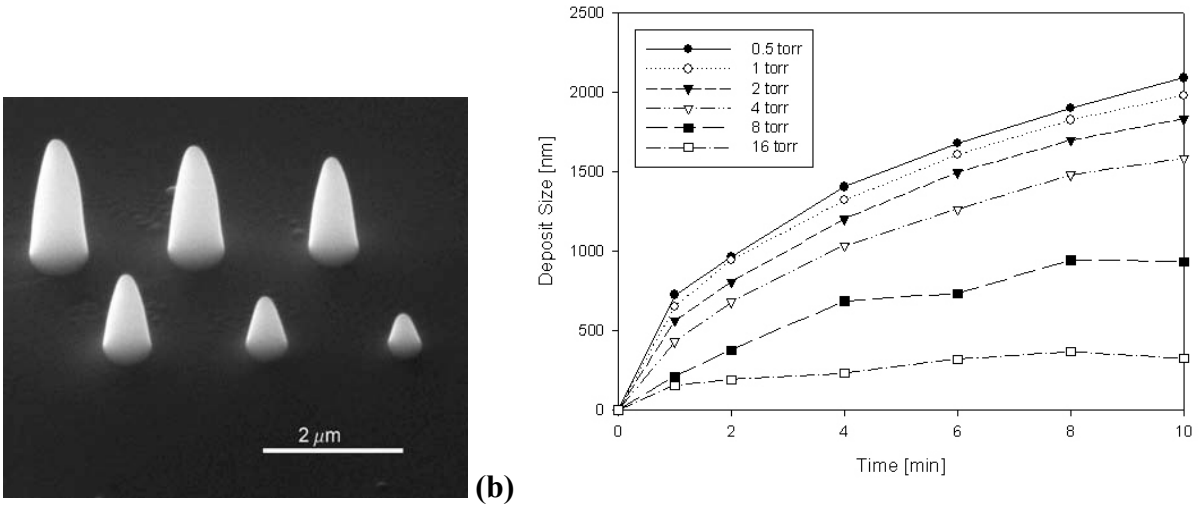

a) **(b)**

Figure 4: Carbon deposition with 30 keV, 5000 pA e-beam at 5.5 mm working distance: (a) SEM micrographs of the 1 torr deposits, (b) Deposit size as a function of time for various chamber pressures.

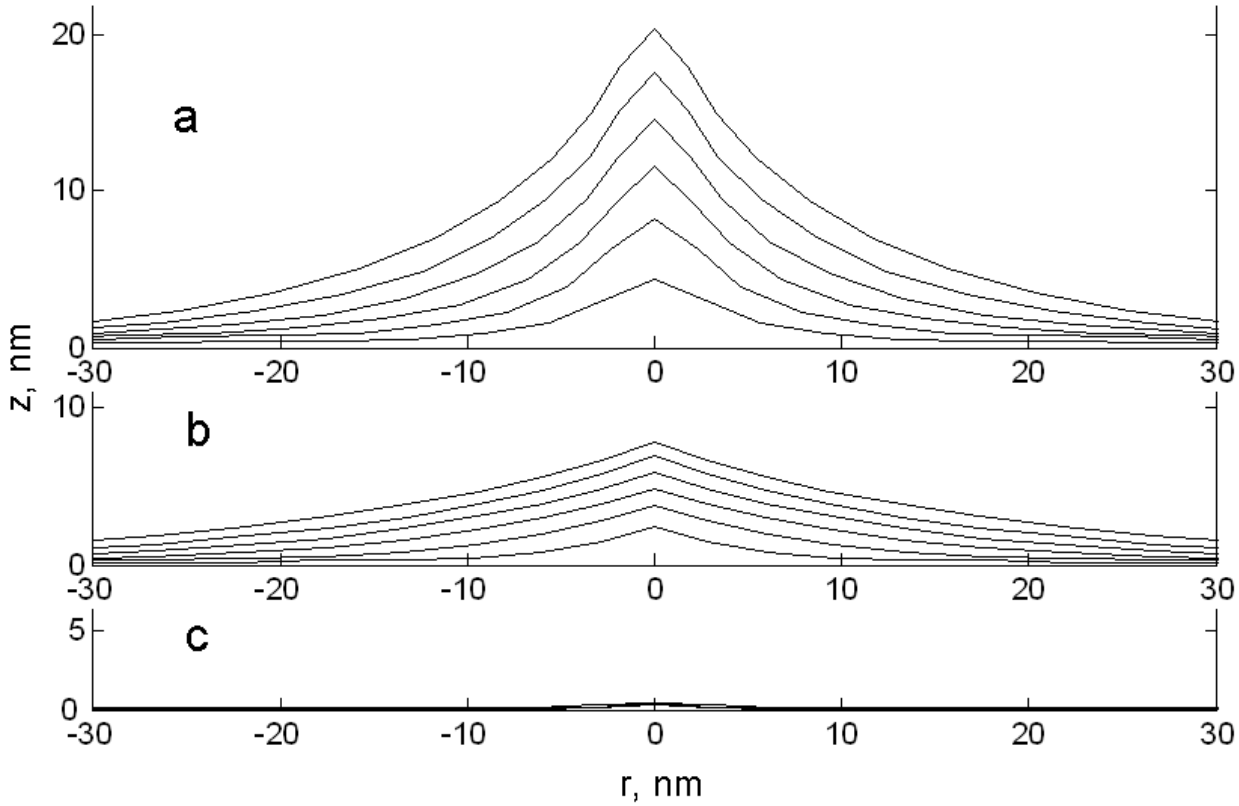

Figure 5: Transient evolution of the deposits for the three growth regimes of (a) reaction-limited, (b) mixed (reaction-diffusion), and (c) diffusion-limited cases, shown in steps of 0.35 s.

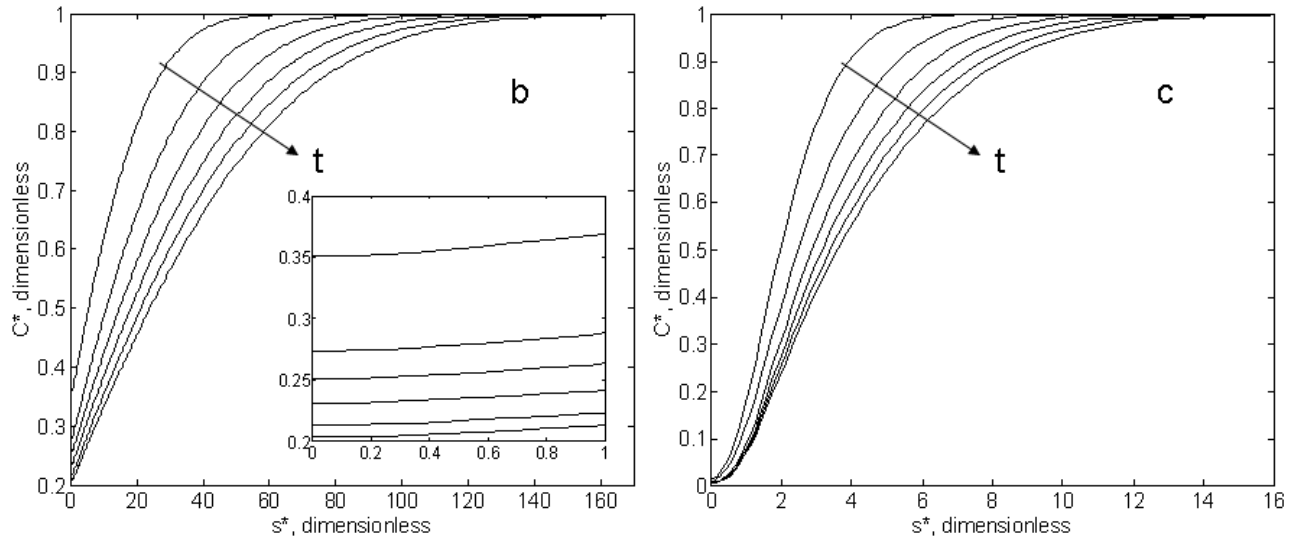

Figure 6: Concentration profiles for the (a) mixed (diffusion-reaction) and (b) diffusion-limited deposition regimes shown in steps of 0.35 s. The insert in Fig. 6 (a) is a magnified view of the concentration field in the vicinity of the symmetry axis of the deposit, clearly showing the vanishing gradient of concentration at r=0.

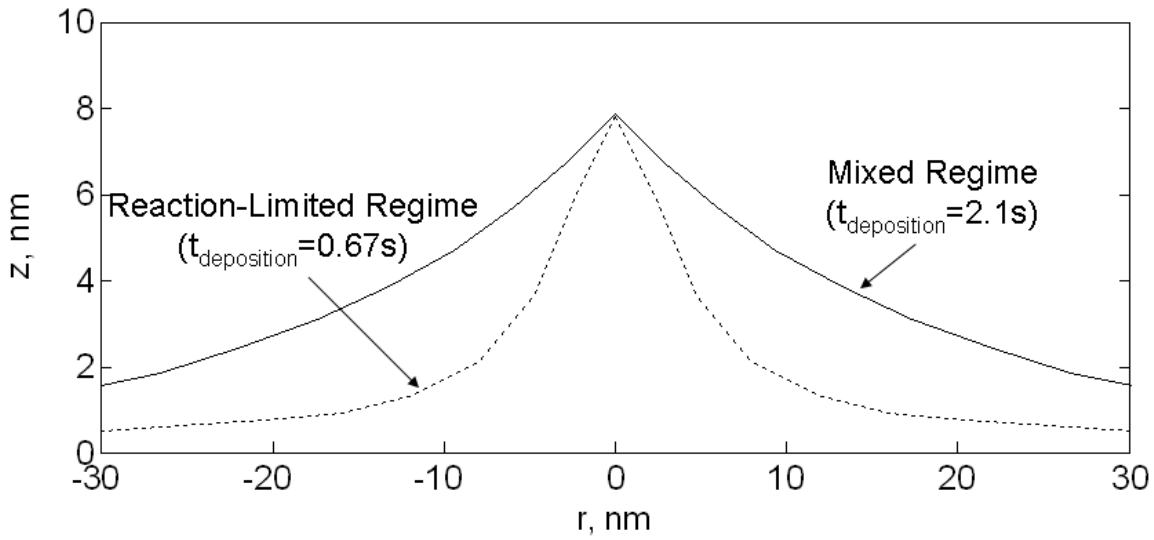

Figure 7. Comparison of deposit shapes simulated for the reaction-limited and mixed (diffusion-reaction) regime grown to the same height. The growth of the mixed regime deposit takes much longer (2.1s) as compared to that (0.67s) for the reaction-limited deposit.

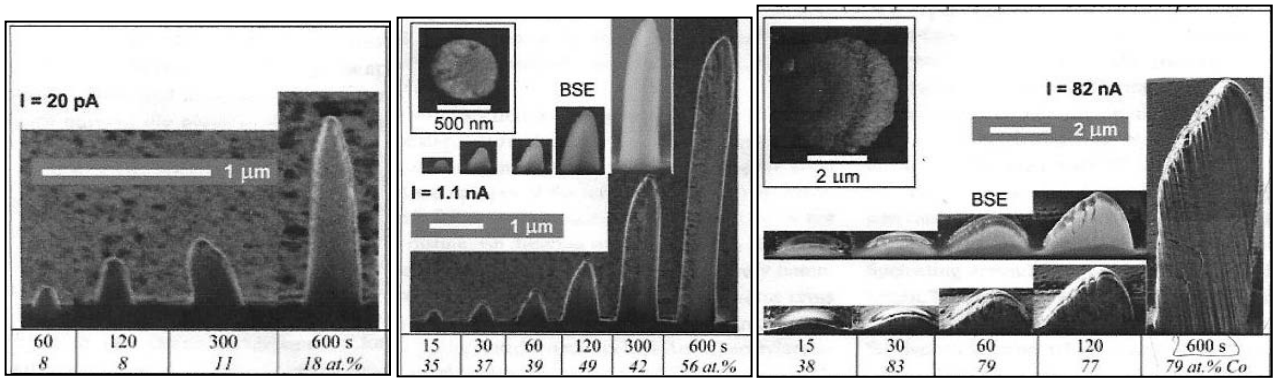

Figure 8: Deposit made by Utke et al. [28] using three different beam currents (20 pA, 1.1 nA and 82 nA) showing an increase in cobalt content and crystallinity.

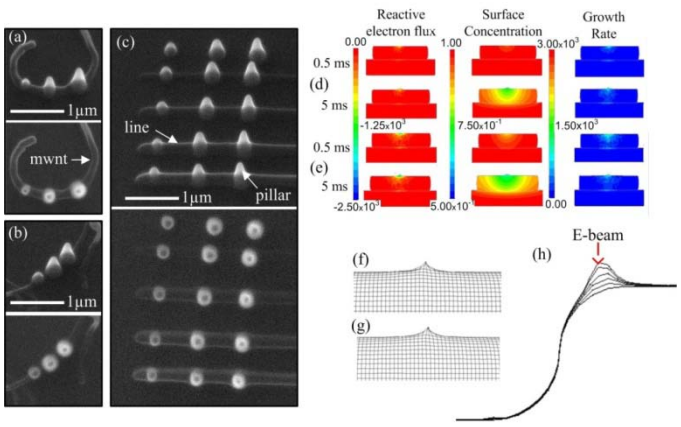

Figure 9. (a-c) 30º and top view SEM images of EBID pillars grown for a period of 1, 3, and 5 minutes on a MWNT with the diameter of (a) 130 nm, (b) 80 nm, and (c) on a bare silicon substrate and the amorphous carbon lines grown by EBID for 2.5, 5, 7.5, and 10 minutes. (d-e) surface distributions (side views along the axis of MWNT) of the reactive electron flux (s^{-1}), precursor concentration and instantaneous deposit growth rate ($nm\text{-}s^{-1}$) for the cases of (d) isotropic and (e) anisotropic secondary electron scattering. (f) simulated deposit shapes after 5 ms of deposition for (f) isotropic and (g) anisotropic secondary electron scattering within the MWNT and (h) example of cross section (cut along axis of MWNT) prolife of an EBID carbon pillar grown at end of MWNT.

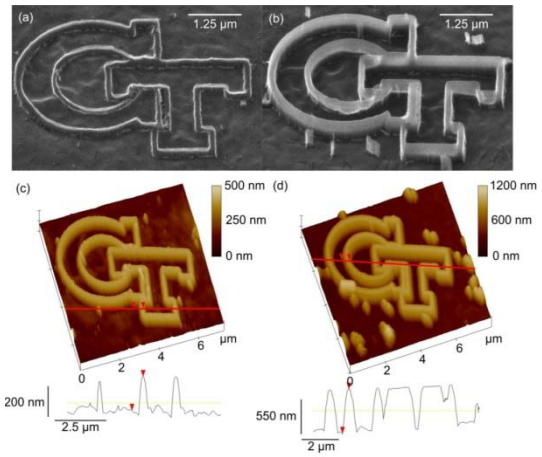

Figure 10. Representative results of high-aspect-ratio nanostructures (GT Logos) fabricated using negative-masking via amorphous carbon EBID-MaCE process of gold-coated silicon substrate. SEM images (under 30º tilt) and AFM topological maps of Si structures formed after 15 (a,c) and 30 (b,d) seconds of etching of EBID-aC/Au-coated samples (Au film thicknesses is 4.7 nm). Due to resist-free nature EBID/MaCE process is simple, flexible and robust alternative to the current state-of-the-art 3D nanofabrication techniques.

Abstract: This research focuses on Electron Beam Chemical Vapor Deposition (EB-CVD) which has an excellent potential for the manufacture of nanoscale materials and devices as well as integrating micro and nanoscale systems. Two different approaches are being pursued. One utilizes a high energy, tightly focused electron beam while another uses diffraction of a low energy broad beam to create patterns. Excellent progress has been made in the deposition of platinum, silicon carbide, and carbon dots, fibers, and lines. Phenomenological relationships between processing parameters and deposition rate and deposit shape have been achieved through extensive statistically designed experimentation. Line uniformity was excellent. Extensive modeling has also provided insight into the deposition process.

1. Introduction and Objectives: Nanoscale materials and devices offer great promise for many applications, but their fabrication often proves problematic. Similarly, integrating nanostructures with microsystems or other nanostructures is one of the main roadblocks to transitioning from single structure fabrication to true nanomanufacturing. This research focuses on Electron Beam Chemical Vapor Deposition (EB-CVD) which has an excellent potential for solving these problems.

An electron beam has been shown to interact with reagent chemicals that are adsorbed onto the surface of a solid substrate causing a chemical reaction(s) that lead to the deposition of a solid metal or ceramic. Importantly, the deposition occurs with minimal heating and thus sensitive substrates or deposits are not thermally damaged. The work of several research groups, including ours [1,2], has established feasibility for nanoscale deposition of several metals and ceramics. Since an electron beam can be focused to spot sizes on the order of 1 nm, it is possible to fabricate truly nanoscale devices.

The goals of the research are to develop focused and broad beam EB-CVD systems, fundamentally understand and model relevant physico-chemical processes, and perform thorough characterization of the structure and properties of deposits. This complimentary approach will permit establishment of the process-nanostructure-property relationships for deposited materials – the key step towards a predictable nanomanufacturing process.

2. Research Accomplishments: Progress has been made in the following three interdisciplinary areas: 1) experimental deposition of platinum, silicon carbide, and carbon using a highly focused electron beam and detailed characterization of the deposits, 2) low energy electron interactions and stimulated dissociation and patterning of $SiCl_4$ multilayers, and 3) modeling of key transport processes controlling EB-CVD.

Platinum and Carbon Deposition: Quantitative process-structure relationships for the EB-CVD of platinum and carbon fibers and lines using an environmental SEM as the electron gun were established. Extensive statistically designed and analyzed experiments defined the influence of beam voltage and current, deposition time, dwell time, and line time on deposition rate, and geometric features such as fiber diameter, line width, and aspect ratio. Beam voltage, current, and precursor replenishment time have been shown to be the key process variables. The statistical regression model permitted prediction of processing conditions that should optimize, i.e., maximize, platinum deposition rate and aspect ratio of nanostructures. The predictions were confirmed through subsequent experimentation. Growth rates up to 0.9 μm/min have been successfully demonstrated for platinum. Carbon deposition rates from methane were slower. Figure 1 shows response contours for the vertical growth rate of platinum fibers. The statistical model we developed [1,2] accurately correlates the growth rate with the process variables as reflected by a correlation coefficient of 97.3% and confirmed by comparison with experimental results shown in the corners of the graph.

These results are significant in that they accurately correlate EB-CVD process variables and geometric attributes of the resulting deposit. Such a correlation is invaluable for the manufacture of nanoscale platinum components. Expected applications include repairs of masks and prototype microelectronic devices, selective coatings for biomedical and chemical sensing devices, nanolaminates, and integrating nanomaterials with microsystems.

Focused EB-CVD of SiC Nanofibers:
SiC nanofibers were deposited with the Focused EB-CVD system using methylsilane as the precursor. Deposition of SiC fibers was demonstrated and investigated as a function of incident beam voltage, spot size, flow rate, and deposition time. The deposits were also analyzed and the microscopic Fourier

transform infrared spectroscopy result shows the TO and LO phonon vibrations of SiC at around 800 cm^{-1} and 1000 cm^{-1}, respectively. This indicates formation of poly-crystalline SiC precipitates. Periodic patterns of SiC fibers were developed for future use.

We have also used the focused ion-beam to "cleave" or "mill" the fiber so that good chemical and structural information can be obtained.

Low Energy Electron Interactions: Previously we demonstrated an enhancement in the deposition of silicon from $SiCl_4$(g) onto a Si(111) substrate due to the presence of 100 eV electron interactions with the adsorbate-substrate system. Electron assisted deposition of metals or semiconductor material has been performed with high energy electron beams. However, inelastic scattering of the primary electron and multiple secondary electron production can amplify the contributions from low energy processes (5 – 100 eV). To fully understand low energy electron interactions in CVD processing, we performed electron stimulated desorption (ESD) experiments on multilayers of $SiCl_4$ condensed on a Si(111) surface. Multilayer experiments allow us to obtain a fundamental understanding of desorption mechanisms from only $SiCl_4$ interactions via eliminating substrate effects. This must be done before moving to the complex $SiCl_4$-Si(111) interface.

Figure 2 depicts desorption products (cations) as a function of the incident electron energy. It can be seen that there is structure in the Cl^+ data which is not present or apparent in any of the other channels. Over this incident electron energy range, $SiCl^+$ and $SiCl_3^+$ have comparable yields whereas the $SiCl_2^+$ and Si^+ yields are smaller relative to the other ions. In addition, there appears to be distinct threshold for these sets of products. At ~ 17eV, Cl^+ and $SiCl_3^+$ are the only observable ions. This is true until 24-25 eV where Si^+, $SiCl^+$, and $SiCl_2^+$ begin to desorb thus the ions are segregated into two distinct thresholds. The mechanisms assigned to these thresholds and the structure in the Cl^+ yield have been assigned to direct ionization, 2-hole states, and 2-hole, 1-electron states. A more detailed discussion can be found in our publication[3].

Besides cation desorption, we have looked at the ESD of neutral atomic chlorine. The ground state chlorine yield is 5.8 times larger than the excited state chlorine yield [4].

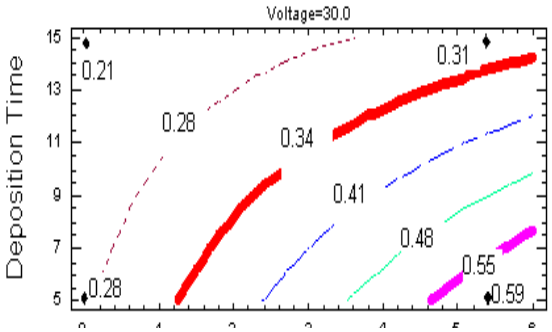

Fig. 1. Contours of constant Pt fiber growth rate (μm/min) as function of deposition time and beam current.

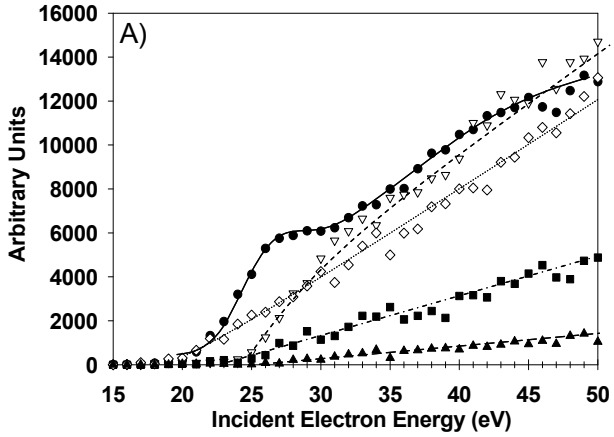

Fig. 2. Cation yields as a function of incident electron energy. Si^+ (▲), Cl^+ (●), $SiCl^+$ (▽), $SiCl_2^+$ (■), $SiCl_3^+$ (◇). The Cl^+ ion yield was divided by a factor of six.

Transport Process Modeling:

Introduction- In FEB-CVD a tightly-focused, high-energy electron beam impinges on a substrate and the high energy primary electrons interact with the substrate to produce low energy secondary electrons (SE). Three methods of precursor gas introduction are common: complete flooding of the reaction chamber with the precursor, flooding of a smaller reaction cell within the chamber and local injection of the gas using a very fine needle. Once on the surface, the molecules redistribute by surface diffusion. Interactions of adsorbed molecules with back-scattered primary and secondary electrons of the appropriate energy result in their dissociation forming a deposit. As the deposit grows, the electron beam also begins to interact with the deposit itself. The deposition reaction mechanism is complex, subject of debates in the literature, and may involve

other factors such as localized substrate/deposit heating and surface electron-phonon-molecule coupling [5]. FEB-CVD has shown promise for nanoscale deposition from a variety of materials [2, 5]. Potential applications include nanofabrication [6, 7], integrated circuit mask repair [8], and fabrication of tips for scanning tunneling and atomic force microscopes [9].

In an attempt to characterize the electron beam chemical vapor deposition process extensive experimentation has been performed under a variety of conditions and with many different precursors. However, limited advances have been made in providing theoretically sound and experimentally validated understanding of the underlying physics. Silvis-Cividjian et al. [10] used Monte Carlo simulation techniques developed for electron microscopy to investigate the role of electron scattering and secondary electron production in the deposit profile evolution. This work was later extended by others [11, 12], but accurate predictions of the deposit growth rate, both qualitative and quantitative, have been elusive.

Chamber Scale Transport- To identify the growth limiting process, a comparison of time scales for relevant physical phenomena can be made. For the precursor molecules, these are the time scales associated with their transport to the substrate τ_T, adsorption onto the substrate τ_A, and deposition reaction τ_R. For the electrons, there is a time scale for transport from the electron source (i.e., the zone within the substrate where secondary electrons are generated) to the deposition zone τ_E. Using typical system parameters and representative precursor(CH_4)/substrate(Si) properties all relevant time scales can be estimated ($\tau_{T-diffusive} \sim 10^{-1}$ s, $\tau_{T-ballistic} \sim 10^{-4}$ s, $\tau_A \sim 10^{-6}$ s, $\tau_R \sim 10^{-5}$ s, $\tau_E \sim 10^{-9}$ s) [10]. Since τ_T is the largest process time scale the precursor transport is the slowest and, therefore, the rate limiting process; and all processes, including precursor transport, can be treated as quasi-steady-state on the observation (growth) time scale ($\tau_O \sim 10^2$ s). With this understanding, we considered two stages of the deposition process [10]: early hemispherical growth upon nucleation and longer-term growth of a cylindrically-shaped deposit with limited lateral broadening. Such experimentally observed deposit shapes are defined by the location of the primary electron scattering, i.e., within an unbounded substrate (hemispherical growth) vs.

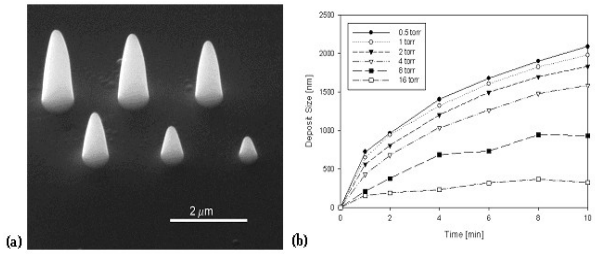

Fig. 3. A 10% methane (precursor) 90% argon precursor flooded into the chamber was used to deposit carbon onto a polished silicon substrate using an FEI Quanta 200 ESEM system. (a) SEM micrographs of the 1 torr deposits obtained with 30 keV, 5000 pA e-beam at 5.5 mm working distance, (b) Deposit size (height) as a function of time for various chamber pressures for carbon deposition with 30 keV, 5000 pA e-beam at 5.5 mm working distance. Deposits were also obtained (not shown) with an electron beam energy of 25 keV and a beam current of 1100 pA. These deposits were fairly cylindrical in shape and have a high aspect ratio. The growth of the 25 keV cylindrical deposits and the 30 keV hemispherical deposits exhibited approximately linear and square-root time dependences, respectively. Reprinted with permission from reference 13.

within the confines of the deposit itself (cylindrical growth) [13].

Figure 3 shows (a) SEM of representative carbon deposits and (b) dependence of the deposit height on the chamber pressure. The size of the deposit decreases with an increase in the chamber pressure (Fig. 3b), ruling out the possibility of the ballistic precursor transport which calls for an increase of the deposit size with pressure [13]. If one considers how pressure affects the primary electron beam current reaching the substrate these results are not surprising. As the electrons pass through the gas-filled chamber they are scattered, depending on the electron scattering cross section of the gas and the distance traveled by the electrons to reach the substrate. Because of the exponential dependence of the scattering on pressure, a significant decrease in the number of electrons reaching the substrate could be expected. This reduced primary current results in a reduced number of "reactive" secondary electrons generated and, in turn, a reduction of the deposit size as the pressure increases. Consistent with the chamber-scale, diffusion-limited mode of deposition, the results (Fig. 3b) exhibit minimal pressure-dependence as the chamber pressure decreases below

1 torr and, therefore, electron scattering is diminished.

Surface Transport- Potential importance of surface diffusion contribution to overall mass transport in FEB-CVD has been suggested in electron beam induced deposition (EBID) of residual hydrocarbon contamination in electron microscopy [14, 15]. With appropriate control of the electron beam, carbon dots and lines [16] as well as sophisticated three dimensional carbon nanostructures [17] have been deposited. Many authors [16], [18], [19] have explored experimental and theoretical aspects of the contamination deposition process, concluding that surface diffusion is the dominant species transport mode. Amman et al. [13] proposed a rudimentary species transport model combined with a simplistic electron scattering model, which did not account for transient spatial distribution of the precursor concentration and dynamic surface evolution effects.

Recently, we have developed a comprehensive dynamic model coupling surface mass transport, electron transport and scattering, and precursor species decomposition to predict deposition of carbon nanostructures [20]. The governing surface transport equation has been derived, generalized by non-dimensionalization, and solved numerically for 1-D cylindrical geometry.

$$\frac{\partial C^*}{\partial t^*} = \frac{t_{obs}}{t_{\text{diff}}}\left(\frac{1}{r^*}\frac{\partial}{\partial s^*} r^* \frac{\partial C^*}{\partial s^*}\right) - \frac{t_{obs}}{t_{\text{sink}}} C^* \dot{Q}^*$$

Here, the starred quantities are dimensionless concentration C^*, time t^*, radius r^* and arc length s^* defining the deposit/substrate surface, and mass sink (reaction) term $\dot{Q}^*$. The relevant time scales include that for diffusion based on the beam width (d_b) as the length scale and surface diffusion coefficient D ($t_{\text{diff}} = d_b^2 / D$), the mass sink (reaction) time scale t_{sink}, given by the inverse of a product of primary electron flux j_{PE} with the secondary electron yield δ_{SE} and maximum dissociation cross section $\sigma_{\max}$ ($= 1/ j_{PE}\delta_{SE}\sigma_{\max}$), and the observation time scale t_{obs} on which growth of deposit occurs. Based on the relative magnitudes of the diffusion (t_{diff}) and reaction (t_{sink}) time scales three distinct growth regimes can be identified. In the case where t_{diff} is less than t_{sink} the deposition reaction is faster than surface diffusion, resulting in a diffusion-limited growth regime. In case $t_{\text{diff}} = t_{\text{sink}}$ surface diffusion is faster than the reaction, resulting in a reaction-limited growth regime. The most general mixed reaction-diffusion growth regime occurs when $t_{\text{diff}} : t_{\text{sink}}$. The three possible deposition regimes have been simulated (see [20] for details) using acetylene adsorbed on Si(100) as a representative precursor-substrate pair [21].

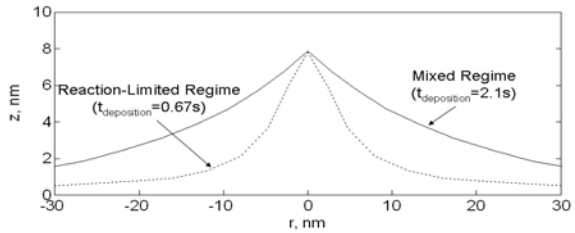

Fig. 4. Comparison of deposit shapes simulated for the reaction-limited and mixed (diffusion-reaction) regime grown to the same height. The growth of the mixed regime deposit takes much longer (2.1s) as compared to that (0.67s) for the reaction-limited deposit. Reprinted with permission from reference 20.

It is important to point out that the vertical growth rate can be a misleading measure of the deposition rate since it depends on the deposit shape. A volumetric deposition rate is shape-independent and far more instructive as a measure of deposition rate [20]. Nanopillars deposited in different deposition regimes not only grow at different rates, but also have different shapes. As shown in Figure 3, when deposition is limited by mass transport not only is the deposition rate slower but in addition much broader structures are formed. The broadening of the nanopillars due to primary electron scattering and secondary electron generation within the deposit [14] does not play a significant role in widening of the shape in the early deposition stages, but becomes important when deposit size is comparable to the electron mean free path.

Thermal Issues- Substrate and deposit heating by the electron beam during FEB-CVD has been hypothesized to affect deposit composition and crystallinity and may also affect precursor transport to the deposition zone. No direct experimental measurements of temperature rise within FEB-CVD deposits are available. Using Monte Carlo electron scattering simulations [22 several simplified thermal models have been proposed [23, 24]. Specific to FEB-CVD, Randolph et al. [24] used electron transport simulations to predict a heat generation term for the steady state heat diffusion equation,

which was then solved numerically. However, the assumption of diffuse transport of the heat carriers is questionable if a characteristic length (e.g., dimension of nanodeposit or size of the energy deposition domain given by the electron beam width) is comparable to the mean free path of the heat carriers, which is the case for FEB-CVD. In such case the heat carriers (conduction electrons in metals and phonons in dielectrics) have to be modeled as discrete particles with their transport described by Boltzmann Transport Equation (BTE). Development of such a transport model is difficult and has not yet been applied to the electron beam heating problem. In this work, a time scale analysis of relevant high energy electron interactions with target materials (both deposit and substrate) and heat carrier transport (both electrons and phonons) is used to estimate thermal perturbation introduced by the electron beam. Copper is selected as a representative material since it is often used as a substrate in electron microscopy imaging and many of the deposited materials are metallic. In the course of scattering in metal, the primary electron looses most energy due to excitation of conduction, valence, and core electrons [25]. The Fast Secondary Electron (FSE) model [22 can be used to estimate a total Inelastic Mean Free Path (IMFP) for these excitation processes. The averaged (0<E<20keV) IMFP for copper is ~8.4 nm and the time scale is $\tau_{PECu} = 1.4 \cdot 10^{-16}$ s. The electron-phonon scattering mean free path and the scattering time can be obtained from the electric resistivity data. For high-purity copper the electron-phonon scattering time $\tau_{e_c - ph}$ equals $2.5 \cdot 10^{-14}$ s, while the mean free path $\lambda_{e_c - ph}$ is ~38 nm [26]. Ziman [27] estimates the free electron-free electron scattering time $\tau_{e_c - e_c} \sim 10^{-12}$ s, which results in a mean free path $\lambda_{e_c - e_c}$ of ~ 1.5 μm (assuming Fermi velocity of $\sim 1.5 \cdot 10^6$ m/s [26]). Calculation of the phonon relaxation time in metals is not trivial. The phonon mean free path in metals depends on phonon-phonon (U-processes), phonon-electron and phonon-defect scattering. However since the temperature of interest (T~300K) is close to the Debye temperature for copper ($\theta_D = 340$ K [26]) the phonon-mean free path can be roughly estimated by neglecting the phonon-electron and phonon-defect contributions. This yields a phonon mean free path λ_{ph} of ~7 nm [27]. Dividing the phonon mean free path by the average phonon speed of 5000 m/s [26] results in the characteristic time for phonon scattering $\tau_{ph} \sim 1.5 \cdot 10^{-12}$ **s**. Comparing all relevant time scales for a primary electron scattering results in $\tau_{ph} \sim \tau_{e_c - e_c} ? \quad \tau_{e_c - ph} ? \quad \tau_{PECu}$. Based on these time scales the proper formulation of high energy electron heating of a metal will involve solution of both the electron and phonon transport equations coupled through the electron-phonon collision integral [28]. The electron transport equation should include an electron source term to account for the perturbation introduced by the excited core and valence electrons. The source time scale τ_s represents time between two primary electrons impinging on the substrate and can be easily computed by dividing the charge of an electron by the electron beam current *I*.

The calculated source time scales for electron beam currents used in experiments by Utke et al. [29] can be used for evaluating expected thermal effects. For electron beam currents up to ~1000 pA $\tau_s \geq 1.4 \times 10^{-10}$ **s** ? $\tau_{ph} \sim \tau_{e_c - e_c}$? $\tau_{e_c - ph}$? τ_{PECu}. In such case both the local electron and phonon distributions will barely be perturbed by a primary electron and will reach equilibrium before another primary electron enters the substrate. In turn, energy dissipated by an individual primary electron over its trajectory within the metal target can be neglected, resulting in negligible heating and temperature rise. With currents in the 10-1000 nA range, the electron source term time scale $\tau_s \sim (5.5 \times 10^{-14} - 1.4 \times 10^{-10})$**s** will be on the same order of magnitude as the phonon relaxation time. In such case the electron beam will start introducing a slight perturbation to the phonon distribution while the electron distribution will reach equilibrium quickly. Thus, in experiments with beam currents in the 10-1000 nA range a moderate and spatially uniform heating and temperature rise can be expected. If electron beam current is greater than ~(1-10) μA the electron source term time scale $\tau_s < 5.5 \times 10^{-14}$ **s** will be of the order of magnitude of the electron-phonon collision time scale or shorter. Such high currents will result in significant perturbation of both the electron and phonon distributions. With both distributions in non-equilibrium a significant heating and increase in target temperature are expected.

Utke et al. [30] have recently shown that beam current can affect both the composition and crystalline structure of the deposits of cobalt from $Co_2(CO)_8$ grown using FEB-CVD. Figure 5 shows cross sections of three different sets of deposits made.

Deposits made using the lowest current (20 pA) have the lowest cobalt content and no apparent crystalline structure. Deposits made at the highest current (82 nA) have a much higher percentage of cobalt and exhibit some structural organization. It has been hypothesized that at high deposit temperatures (>100 C) more $Co_4(CO)_{12}$ is converted to metallic cobalt which results in a more pure cobalt deposit. Higher temperatures could also provide the energy for rearrangement of the deposited cobalt into a more favorable crystalline structure. Experimental finding of Utke [29, 30] support theoretical time scale analysis predictions. Currents of ~(20-1000) pA correspond to limited heating and, therefore, low metallic cobalt concentration. Whereas the currents higher than ~100 nA result in significant heating and an increase in cobalt concentration as well as deposit crystallinity.

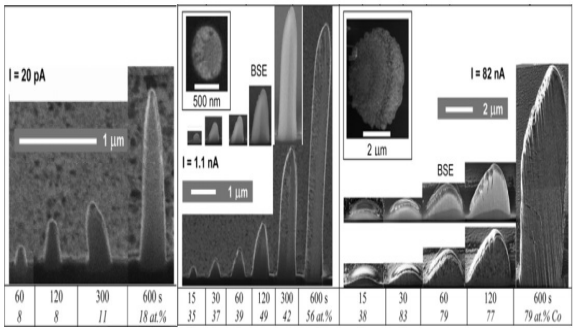

Fig. 5. Deposit made using three different beam currents (20 pA, 1.1 nA and 82 nA) showing an increase in cobalt content and crystallinity. Reprinted with permission from reference 29.

Similar time scale analysis can be performed for crystalline dielectric and semiconducting materials such as silicon or carbon. Silicon will be used as a representative material since it is often used as a substrate in EB-CVD experiments and its well studied electronic nature. As in the case of metals accurate computation of all steps in a cascade of inelastic electronic scattering events is difficult due to lack of complete sets of relevant experimental data, and instead the FSE model can be used to estimate a total IMFP. With ρ=2.3g/cm^3, Z=14, and A=28.8 g/mol the averaged ($0 \le \boldsymbol{E} \le 20$ keV) IMFP for silicon is ~30 nm and the representative time scale is $\tau_{PESi} \sim 5\times10^{-16}$ s. Pop et al. [31] calculated electron-phonon scattering rates for conduction electrons based on the standard Fermi Golden rule. Taking an inverse of the scattering rates we obtain the phonon emission/scattering time scale $\tau_{e_c-ph} \sim 10^{-13} - 10^{-14}$ s. According to Zhang [26] the phonon mean free path λ_{ph} and scattering time τ_{ph} in pure silicon crystal at 300 K are 45 nm and 7.7×10^{-12} s, respectively. Comparing all relevant time scales for the primary electron-target interactions yields τ_{ph} ? τ_{e_c-ph} ? τ_{PESi}, which suggest the following physical interpretation: the primary electrons lose its energy to excite core and valence electrons to the conduction bands; the conduction band electrons then relax to its equilibrium electronic energy to heat via electron-phonon scattering. The final step of the energy cascade is thermal equilibration via phonon-phonon scattering.

Given the results of the time scale analysis, the BTE with a source term due to electron-phonon and phonon-phonon coupling is an appropriate model to describe electron beam heating of a crystalline dielectric. As in case of metals the appropriate time scale for the source term τ_s is the time in between two primary electrons impinging on the substrate and can be easily computed by dividing the charge of an electron by the electron beam current I. For electron currents up to ~1000 pA the source term time scale will be much greater than all other time scales involved. In such situation the phonon distribution will reach equilibrium and the heating and temperature rise introduced by the primary electrons will be negligible. With currents in the 10-1000 nA range the electron source term time scale τ_s will be of the same order of magnitude as the phonon relaxation time τ_{ph}. In such a case, a weak energy source term in BTE will slightly perturb the phonon distribution resulting in moderate heating and temperature rise. If the electron beam current is greater than ~1-10 µA the phonon source term time scale will be of the order of magnitude of the electron-phonon collision time scale or shorter. Such high currents will result in significant perturbation phonon distributions, which does not have sufficient time to relax to its equilibrium state, and thus significant deposit/substrate heating and increase in temperature should be expected.

Finally, evaluation of EB induced heating in disordered solids such as amorphous carbon is much more difficult than in the case of crystalline materials. This is mainly because amorphous carbon exists in a wide variety of forms with microstructure and physical properties that depend on minute detail of the synthesis/deposition method [32]. The electronic conduction mechanism depends on the specific type of the amorphous carbon, and likewise is the phonon transport [33]. Unfortunately, this information for amorphous carbon deposited via EB-

CVD literature is lacking at the moment [34-39], making it difficult to identify the specific energy transfer cascade and to perform a time scale analysis.

Modeling Conclusions- The modeling has demonstrated the importance of theoretically sound treatment of heat and mass transfer issues in FEB-CVD. We also reviewed the state-of-the-art modeling approaches supported by experimental results.
Our model includes treatment (ballistic vs. continuous) of the chamber scale precursor transport, which results in differentiation in time and pressure dependence of the deposit growth rate. Theoretical analysis of contamination deposition shows that surface diffusion affects both the growth rate and shape of the deposited nanopillars. In the most general case of FEB-CVD when all mass transport modes are of importance, surface diffusion will be one of the key factors defining the shape as well as the growth rate. Finally, the deposit heating is an important factor, which influences the nature and crystallinity of the deposit as well as surface transport properties affecting the growth rate. Although current understanding is incomplete, the scaling analysis provides a route for qualitative assessment of the expected deposit properties depending on the magnitude of the electron beam current. It should be emphasized that the reported results are obtained for a "typical" representative FEB-CVD system, and should be used as a guide rather than a cast-in-stone recipe when applied to a specific system and different deposition conditions.

Microstructural Characterization:
Atomic Force Microscopy (AFM) of electron-beam deposited micro-ring structures- Micron-ring structures are formed due to primary, secondary, and backscattered electron induced deposition of residual hydrocarbons adsorbed on the surface of a Si wafer. A systematic analysis of the dimensions of these rings reveals that the heights, widths, and diameters are influenced by the e-beam intensity and working time. A typical AFM image of a ring is shown in Figure 6. The generation of such rings can be explained by the two-dimensional surface diffusion process of the absorbed hydrocarbons.

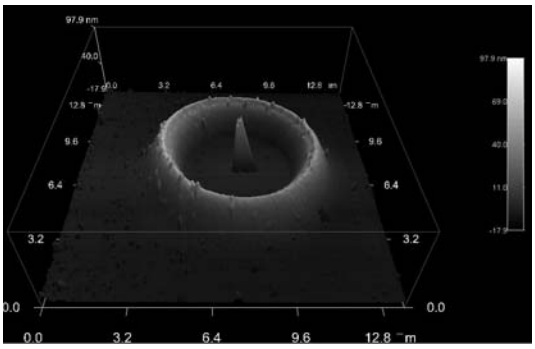

Fig. 6. Electron beam deposited ring.

Dynamic Growth of 3-d Carbon Nanostructures and nanowelding Using EBID:

Executive Summary
Electron Beam Induced Deposition (EBID) of hydrocarbon residuals, with appropriate electron beam control, can provide a basis for 3-D nanofabrication. In this process solid carbon deposits are formed due to interaction of primary and secondary electrons with residual hydrocarbon species adsorbed on the surface of the substrate. The emphasis of research in this area has been on experimental demonstration of various deposited nanostructures, and there is a growing need for theoretically rigorous and experimentally validated analysis to gain fundamental insight into the basic physics and chemistry of EBID. In this work, we explore the formation of secondary ring-type microstructures around nanopillars produced by electron-mediated decomposition of residual hydrocarbon contamination on a semiconducting substrate, via synergetic combination of multiphysics/multiscale simulations and carefully designed deposition experiments [40]. Armed with this fundamental insight, we also describe a new method by which the EBID-generated ring-type deposit can be used to indirectly bond nanoscale objects to the substrate. The proposed method is experimentally demonstrated by bonding Multiwall Carbon Nanotubes (MWNTs) to a Si(100) substrate.

EBID Experiments
We have performed a series of experiments studying the EBID of carbon nano-pillars using adsorbed residual hydrocarbons as a precursor. The deposition experiments were performed using an FEI Quanta 200 Environmental Scanning Electron Microscope (ESEM), and resulting deposits were imaged using Asylum Research's MFP-3D Atomic Force

Microscope (AFM). A polished Si(100) wafer cleaned for 30 seconds in 6:1 Buffered Oxide Etch was used as a substrate. The experiments were performed in high vacuum (~10^{-6} Torr) with no additional precursor gases introduced. The deposits were formed by keeping the focused electron beam stationary for a time period of 2.5 to 25 minutes with electron beam accelerating voltages in the range of 15 to 30 keV and corresponding currents of ~350 to 450 pA. The beam angle of incidence was varied between 0 and 45 degrees, as measured from the normal to the substrate surface.

EBID simulations

The EBID precursor dissociation reaction rate can be calculated as:

$$\dot{Q}(s,t)=\int_0^E \sigma_d(E)C(s,t)j_{se}(E,s)dE=C(s,t)\int_0^{E_{max}} \sigma_d(E)j_{se}(E,s)dE=C\dot{Q}'' \quad (1)$$

where $C(t,s)$ is the surface concentration of the precursor at time t and position s, $\sigma_d(E)$ is the deposition reaction cross section in units of area per electron, and $j_{se}(E,s)$ is the flux of secondary and backscattered electrons with energy E arriving to the deposition surface at the location s, in units of electron per area and time. Equation (1) indicates that the rate of deposit growth is defined by a product of local concentration of adsorbed precursor $C(t,s)$ and local flux of reactive electrons $\dot{Q}_1''$. The Surface Transport Equation (STE) for adsorbed species we developed in our previous work [41] was used to predict the local concentration $C(t,s)$ of adsorbed precursor species. The spatial distribution of the reactive electron flux $\dot{Q}_1''$ depends on the primary electron scattering within the substrate and deposit. We used a single electron scattering Monte Carlo model to predict the backscattered and secondary electron distributions. The basic algorithm is described in our previous work [41], but two important modifications have been introduced in this work to achieve quantitatively accurate predictions: (1) the empirical equation for the total elastic cross section was used as proposed by Browning et al. [42] for elastic scattering of primary electrons with energies below 10 keV; and (2) the simulation domain was significantly extended to 20 μm in both radial and depth (into the substrate) directions to properly account for all "reactive" electrons reaching the substrate. An approach suggested by Fowlkes et al. [43] was used for approximation of the deposition reaction cross section: that is an electron impact dissociation cross section was applied for electron energies below the threshold energy, corresponding to intersection of the ionization and dissociation cross section curves for the precursor, and, for electron energies beyond the threshold, the electron impact ionization cross section was used for computing the dissociation reaction rate (Eq. 1). The Alman et al. [44] model was used to approximate the electron impact dissociation cross section, while experimental data from Kwitnewski et al. [45] were fitted to a model suggested by Fowlkes et al. [44] to approximate the ionization cross section. The cross sections for C_4H_6, a representative residual hydrocarbon contamination, were used in all simulations. The reactive electron flux was computed with a cutoff energy of 7 keV for secondary and backscattered primary electrons predicted by Monte Carlo simulations.

In order to properly simulate the EBID experiments with angled incidence of an electron beam (and resulting asymmetric electron flux and deposits), the two-dimensional surface diffusion of the adsorbed hydrocarbon precursor and three-dimensional growth of the deposit models have to be employed. While extension of the STE to two-dimensions (in topological coordinates fitted to the surface of substrate/deposit) is straightforward, simulation of the deposit surface evolution in three dimensions is simple theoretically, but can be very cumbersome computationally. In order to simulate a realistic shape of the deposit in 3D, a much higher number of primary electrons need to be simulated to obtain a reasonable spatial distribution of the reactive electron flux $\dot{Q}_1''(x,y)$. This puts significant demand on required computational resources, and so we limited our work to simulation of the instantaneous growth rate of nanostructures at the early deposition stages. In such a situation, a flat surface approximation can be used for both the electron and mass transport models with no sacrifice in accuracy and realism of simulations. For the electron transport this implies ignoring the effect of the vanishingly small (relative to the substrate) nanostructure in Monte Carlo simulations, and for the precursor mass transfer a 2-D version of the STE, with appropriate boundary and initial conditions, was solved on the surface of the substrate:

$$\frac{\partial C}{\partial t}=\frac{\partial}{\partial x}\left(D\frac{\partial C}{\partial x}\right)+\frac{\partial}{\partial y}\left(D\frac{\partial C}{\partial y}\right)-C\dot{Q}_1''$$

$$B.C.\ \ C\big|_{y\to\pm\infty}=C_\infty \quad C\big|_{x\to\pm\infty}=C_\infty$$

$$I.C.\ \ C(t=0,x,y)=C_0(x,y) \quad (2)$$

Where x and y are planar coordinates on the surface of the substrate, C_∞ and C_0 are the far-field and

initial surface concentrations of the precursor, respectively, assumed to be the same in all reported simulations. Equation 2 was discretized using the Finite Volume Method and the resulting system of linear algebraic equations was solved using the Alternating Direction Implicit (ADI) method.

Results and Discussion

Ring and pillar deposits at normal-to-substrate electron beam incidence

Figure 7 shows an AFM image of a nanopillar-within-a-micro-ring deposit formed by EBID with accelerating voltage of 15keV, beam current of 376 pA, and deposition time of (a) 5 minutes and (b) 25 minutes. During the early stage of the deposition process only the dot/pillar like nanostructures were produced at the point of impact of the electron beam. In later stages, a secondary ring-like deposit began to form around the initial deposit. Specifically, at the 5-minute deposition time (Fig. 7a) height of the ring deposit (~8 nm) is less than half of the center pillar height (~20 nm). However, at the 25-minute deposition time both the ring and center deposit reach about an equal height of ~90 nm. We have also experimentally observed that the height of the central deposit increased linearly with time, while the peripheral ring grew exponentially with time. The diameter of the deposited micro-ring showed linear dependence on the electron beam accelerating voltage, increasing from ~3.5 μm to ~10 μm as the voltage increased from 15 keV to 30 keV.

Early growth deposition was simulated using a methodology described previously in the simulation section with a mass sink (reaction) term (Eq. 1) computed for a Si(100) substrate using 10^6 primary electrons. The estimates for initial concentration ($C_0 = C_\infty \approx 0.25$ μg/cm^2) and surface diffusion coefficient ($D \approx 7.5\text{x}10^4$ nm^2 / s) of the adsorbed residual hydrocarbons were obtained by calibration of simulated results against experimentally observed growth of the central nano-pillar. Figure 8a shows deposit profiles predicted in time steps of ~45 seconds with a final deposition time of 5 minutes for the beam accelerating voltage of 15 keV and electron beam diameter (full width at 50%) of 200 nm. To better illustrate the mechanism of ring formation Figure 8b shows the spatial distribution of the scaled reactive electron flux ($\mathcal{Q}_1^{\&"}$), dimensionless precursor concentration ($C(t,s)$), and the resulting dissociation (deposition) reaction rate given by a product of the former two terms (Eq.(1)). Formation of the ring deposit in Figure 8a can be readily explained by the secondary peak of the dissociation

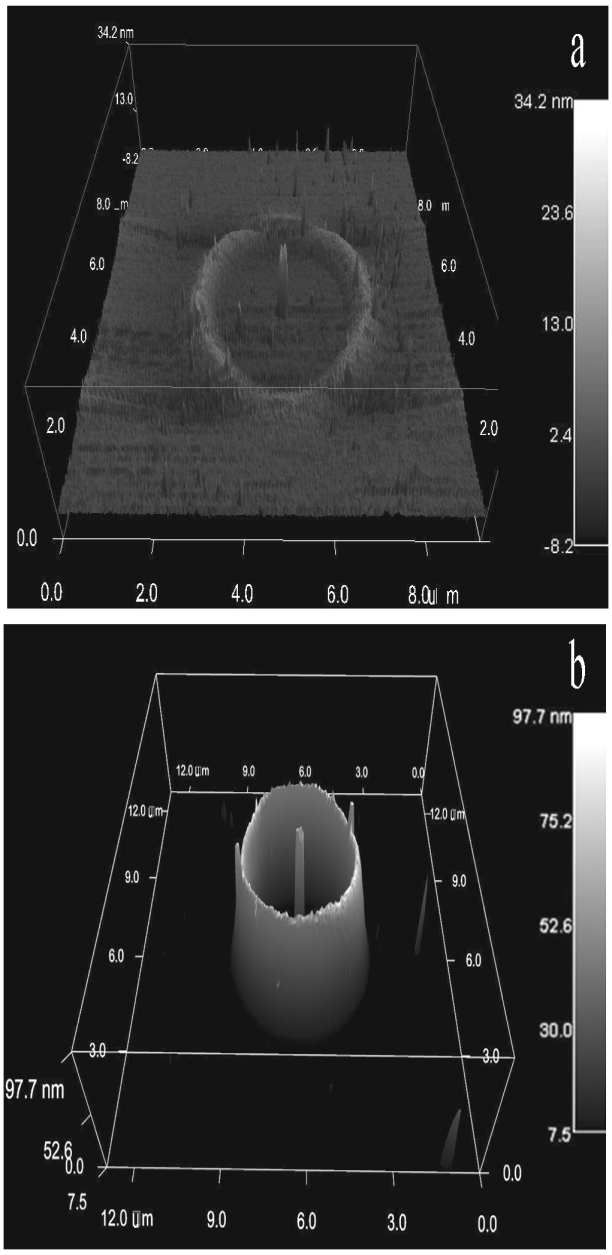

Fig. 7. AFM images of a pillar-within-a-ring deposit formed via EBID with accelerating voltage of 15keV, beam current of 376 pA, and deposition time of (a) 5 minute and (b) 25 minutes. (The planar axes have units of micrometers and the vertical axis has units of nanometers.)

(deposition) reaction rate at around radius *r*~1500 *nm*, resulting from convolution of the secondary and backscattered electron distribution and the concentration profile of adsorbed precursor molecules established by surface diffusion.

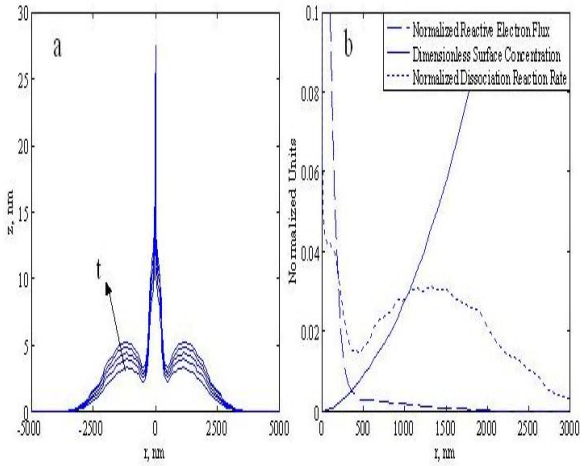

Fig. 8. (a) Transient deposit profiles predicted in time steps of ~45 seconds (final deposition time of 5 minutes), (b) Illustration of ring formation mechanism by showing radial distribution of normalized reactive electron flux, dimensionless surface concentration of precursor molecules, and normalized dissociation reaction rate.

To investigate the effect of the beam energy, the dissociation (deposition) reaction rates for accelerating voltages of 15, 20, 25, and 30 keV were also simulated. Consistent with experimentally observed growth of carbon micro-ring, the radial distance between the center of the electron beam and the predicted secondary reaction rate peak increased linearly with an increase in accelerating voltage. Experimental data and simulation results are compared in Figure 9. The concentration of surface adsorbed precursor molecules near the center of the electron beam reaches a quasi-steady state within a short time period after beginning of the deposition process. The time necessary to reach the quasi-steady state depends on the surface diffusion coefficient D, magnitude of the reactive electron flux $\mathcal{Q}_1''$, and the initial precursor concentration C_0. For the set of EBID conditions presented in this paper, a quasi-steady state concentration is reached within ~30 seconds of the beginning of the deposition process. Changes in the reactive electron flux depend on the growth rate of the deposit, which occurs on a much longer time scale (~minutes) than the changes

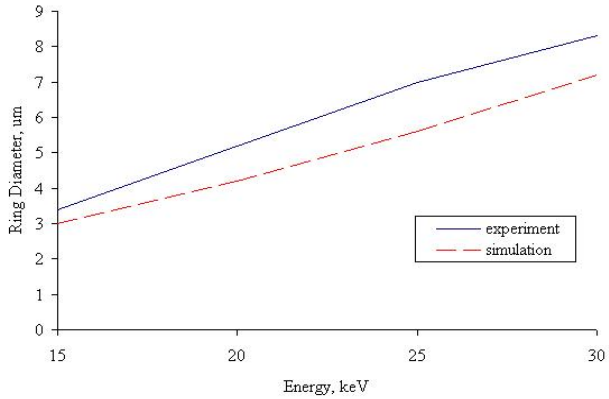

Fig. 9. Comparison between experiments and theoretical predictions of the micro-ring deposit diameter as function of the beam accelerating voltage.

in the surface concentration (~seconds). Thus, beyond the initial transient surface spreading of the precursor, both the local surface concentration and reactive electron flux in the center of the deposit do not change appreciably on the ~second timescale, resulting in a constant growth rate of the central nanopilar (Eq.1). A constant growth rate at the center implies a linear time variation of the nanopillar deposit height, which agrees with our experimental observations.

To gain an insight into further stages of the deposition process the reactive electron flux was simulated for the final shape of the deposit shown in Figure 8a. Figure 10 shows the spatial distribution of the scaled reactive electron flux ($\mathcal{Q}_1''$), dimensionless precursor concentration ($C(t,s)$), and the resulting dissociation (deposition) reaction rate for the late stage growth of the hybrid nanopillar-microring deposit. In contrast to the initial growth (Fig.8b), during the further stages of the growth process (Fig.10) the dissociation (deposition) reaction rate is greater at the location of secondary peak (r~1500 nm) than in the center of the electron beam. This theoretically predicted increase in the relative growth rate of the ring deposit with time, as compared to the centrally-grown nanopillar, is consistent with the experimentally observed trends.

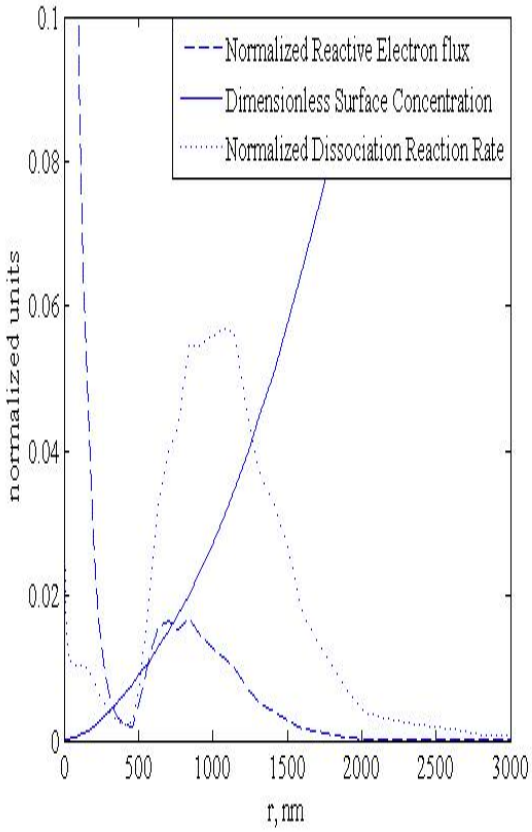

Fig. 10. Reactive electron flux, dimensionless precursor surface concentration, and normalized dissociation reaction rate for the nano-pillar and ring like deposit (simulations for the final deposit profile shown in Fig. 8a)

Ring-type and pillar deposits at varied angles of electron beam incidence

Experiments performed with varied angle of incidence of the electron beam resulted in formation of the ring-like structures, although slightly elongated along one axis, which surrounded nanopillars whose shape and location varied depending on the beam direction. The more oblique was the electron beam direction of incidence with respect to the substrate the further away was the location of the pillar-like deposit relative to the center of the ring microstructure (Figure 11a-c). In addition, the nano-pillar deposits formed a cut-crater like structure, clearly visible in Figure 11g. We performed simulation of the growth rate of EBID structures to gain an insight into the physics of the process, which governs the peculiar behavior observed experimentally. Figure 11d-f shows theoretically predicted instantaneous growth rate for three different angles of incidence five minutes into the deposition process. The reactive electron flux was computed using 1.5×10^7 primary electrons in the beam impinging on a flat substrate. The simulations were performed with the same representative values for the surface diffusion coefficient and initial precursor concentration as in the previously discussed case of normal electron beam incidence. As it is apparent from side-by-side comparison of experiments (Fig. 11a-c) and predictions (Fig. 11d-f), the simulations were remarkably successful in predicting the observed experimental trends: that is both the cut-crater like topology of the nanopillar and also the shift in its location within the micro-ring with an increased angle of electron beam incidence are fully captured in the calculations.

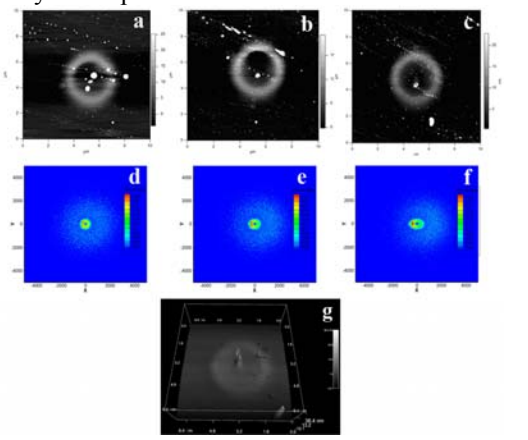

Fig. 11. 2D AFM-imaged topological maps of the pillar-within-a-ring deposits formed via EBID with accelerating voltage of 15keV, beam current of ~350 pA, and deposition time of 15 min. The electron beam angle of incidence is (a) 15°, (b) 30°, (c) 45°as measured relative to normal to the substrate (The planar axes have units of micrometers and the color map denotes vertical elevation in units of nanometers). *Instantaneous deposit growth rates simulated at five minutes into the deposition process, produced for the same electron beam settings as those used in experiments and electron beam incident angles of (d) 15°, (e) 30°, (f) 45°. (Growth rate has arbitrary units and the planar axes have units of nanometers). (g) 3-D AFM image of the EBID deposit produced in the case of 45° electron beam incidence angle, showing topological details of the cut-crater like shaped nanopilar surrounded by a slightly distorted micro-ring.*

It is important to note that these simulations have been performed for the early growth stages when the changes in the surface topology and material property due to deposition do not affect significantly the outcome of both electron scattering and mass transfer calculations, and therefore ignored in the simulations. It is quite remarkable that even such a simplified theoretical treatment can capture fine detail of the deposition process.

Indirect bonding (nanowelding) of nanoscale objects using EBID of residual hydrocarbons

Recently Moskalenko et al. [46] demonstrated that a 10 nm layer of amorphous carbon film deposited using EBID of residual hydrocarbons results in a strong bond between a three-dimensional nanoscale object and a substrate. Specifically, the authors established a carbon bond by scanning the primary electron beam over the Fe-Co-Ni nanoparticle placed on the graphite surface. The amorphous carbon film formed beneath the nanoparticle (in the area referred to by the authors as the geometrical shadow) due to secondary electron scattering within the substrate. However, such an approach may result in significant and potentially undesired deposition (coating) of amorphous carbon in the areas around and on the object that is being bonded to the substrate (due to surface diffusion of adsorbed precursor molecules, reacting with secondary electrons generated within the nano-object). As an alternative bonding strategy, we explore the use of the ring-type deposits for bonding the nanostructure to the substrate, as schematically shown in Figure 12. Such an approach does not involve potentially damaging interactions between the high energy electron beam and an object that is being bonded, as all electrons contributing to the deposition (true secondary and backscattered primary) emerge from the substrate directly underneath of the object, thus localizing bonding contact area.

Figure 13a shows an SEM image of the MWNT bonded to the Si(100) substrate via the ring-type EBID carbon deposit formed underneath the nanotube. To investigate structural stability and mechanical strength of the EBID-enabled carbon bond, we performed a series of simple tests on the bonded MWNT-substrate pair investigating its response on the mechanical load applied with an AFM tip. The nanotubes were first located via tapping mode imaging and then were forcefully displaced by the scanning cantilever tip by switching into the contact mode of AFM. In particular, Figure 13b shows an AFM image of the bonded MWNT prior to an attempt to forcefully displace it using the

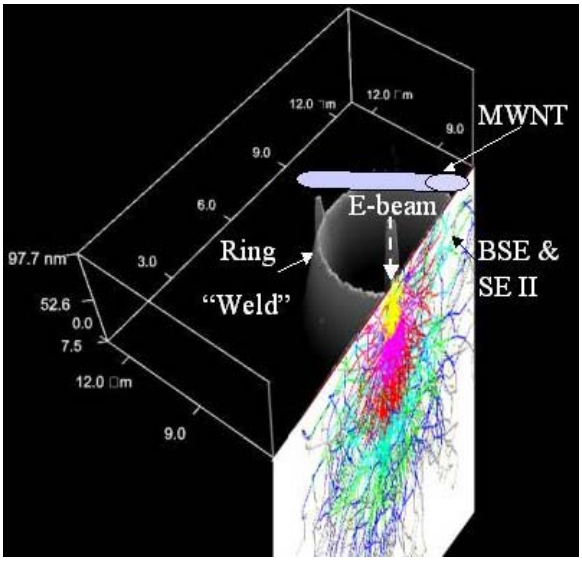

Fig. 12. Schematic of the bonding technique involving secondary and backscattered primary electrons only (electron scattering visualization was done using Leigh 2001 software).

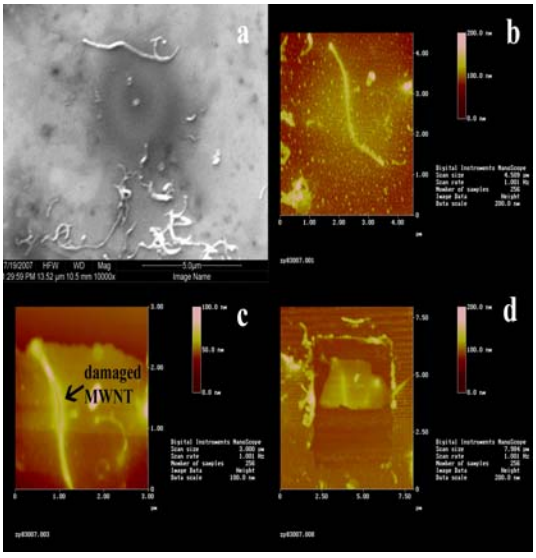

Fig. 13. (a) SEM image of a carbon nanotube bonded to the Si substrate via the ring-type carbon deposit, and AFM images (topological maps) of the bonded nanotube (b) before the AFM bond strength tests, (c) after the first bond strength test, resulting in rupture of part of the nanotube, and (d) after the second bond strength test, resulting in fracturing the substrate underneath the bond.

AFM cantilever tip, which clearly shows a structurally-sound nanotube sitting on the silicon substrate. The first attempt at moving the bonded nanotube resulted in cutting a part of it out due to the sharpness of the AFM tip (Fig. 13c). In the second attempt to move the nanotube (a smaller residual piece of it, which was left over from the first test), the nanotube remained intact and application of the greater AFM force ($\geq 3\mu N$) resulted in ripping off a part of the substrate surface (Fig. 13d). Displacement of an unbonded nanotube by the AFM tip required three times smaller force ($\sim 1\mu N$) to overcome intrinsic tube-to-substrate adhesion and capillary forces and was also accompanied by cutting the tube into pieces by the sharp cantilever tip (the cutting of the nanotube by the AFM tip appears to be common for the contact-mode AFM operation using mechanically stiff cantilevers with a sharp tip). These results demonstrate that the indirect-EBID-formed carbon bond is at least as strong as the Si (100) substrate and the carbon nanotube itself.

Conclusion

In summary, we report on investigation of the transient formation of hybrid, topologically complex microring-nanopilar deposits in EBID of residual contaminants through complimentary experimental and theoretical efforts. In particular, we experimentally demonstrate that the height of the centrally-located nanopillars increases linearly with time, while the microrings surrounding the nanopillars grow exponentially with time. The linear time dependence of the deposit growth at the point of electron beam impact is theoretically explained byrecursor concentration on the surface of the substrate rapidly reaching the quasi-steady distribution with concentration magnitude several orders of magnitude smaller at the center (pillar) point than in the ring region. After initial nucleation phase, as the deposit starts forming the reactive electron flux spatial distribution changes due to difference in the structural topology and chemical composition (material of the deposit vs. substrate) of the irradiated surface. In the central region, the reactive electron flux slightly increases but does not result in a significant nanopillar growth due to highly depleted surface concentration of the precursor; in the periphery, where the ring is formed, the precursor concentration is much higher and even a small increase in the reactive electron flux causes a significant increase in the deposition rate. As the electron beam angle of incidence was increased (measured from the normal to the substrate) the nanopillar-microring formation was still observed, but the nanopillar deposits grew further away from the ring center. Also, the pillar-like nanostructure in the center transformed into a cut-crater like nanostructure. Simulations predicted that the locations of both the microring and the cut-crater like nanostructures are the direct outcome of the asymmetric distribution of the reactive electron flux and the surface concentration of the precursor molecules induced by angled irradiation by the primary electron beam. Remarkable agreement between simulations and experimental results supports the credibility of the suggested physical scenario for EBID of residual hydrocarbons on a semiconductor substrate, thus emphasizing the importance of surface mass transport and higher energy backscattered primary electrons in accurately predicting the complex shape and growth dynamics of deposited nanostructures. Finally, by exploiting the fundamental insight developed through EBID experiments and simulations, we demonstrated a new indirect technique for "gentle" bonding of nanostructures to the substrate, which has potential for applications in nanoscale manufacturing and assembly using electron beam chemical vapor deposition.

EBID APPLICATIONS- EBID-ENABLED MWNT INTERCONNECT FABRICATION:

Executive Summary

With miniaturization of copper based integrated circuits reaching their limit [47], alternative materials are needed. Carbon nanotubes' (CNT) exceptional electrical and thermal transport properties as well as superior mechanical durability make them an attractive alternative to copper [48-50]. The high contact resistance of the CNT-metal conductor interface [48,51] presents the key technological hurdle impeding implementation of CNTs as interconnects. Methods frequently applied for lowering of the CNT-conductor contact resistance either are not applicable to the typical interconnect configuration [52-55] or do not establish contact with inner shells of the Multiwalled nanotubes (MWNT) [48,56,57].

Application of Electron Beam Induced Deposition (EBID) of carbon [58-60] CNT-electrode interface has potential to resolve the above-mentioned issues. In this process a solid deposit is formed at the point of impact of the electron beam due to the decomposition of residual hydrocarbon species adsorbed on the solid substrate [61]. While the application of EBID of amorphous carbon (a-C) for improved CNT-electrode interface has been utilized before [58,59,62-67], little attention has been

dedicated to fundamental understanding of the deposition process and selection of optimal process settings such as electron beam energy, current, geometry, and deposition time and their influence on the interface geometry and resistance. This is the subject of our work related to EBID applications to nanoelectronics.

In order to prepare the sample for EBID processing, individual tubes with proper lengths and diameters must be separated from bundles by in-solution dispersion, aligned between electrodes, and cut at the ends (to expose the inner shells). To avoid hot spots creation and ensure minimal resistance of the interconnect devices CNTs with minimum number of defects should be utilized. The electrode design and fabrication must accommodate for tube alignment methods utilized and ensure the durability of the deposited metal films. To estimate the crucial electron beam condition such as the energy, current, geometry, and time ON necessary for growth of the desired geometry, a-priori prediction of the EBID process is needed. For such a procedure, validated growth simulation and method for estimation of the adsorbed species surface diffusion coefficient (D_s) and representative concentration (C_0) are needed. Finally, to achieve the above characteristics of the interface, the amorphous a-C as deposited by EBID must be transformed into partially or fully graphitized form. The following subsections briefly summarize the work performed for each of the above aspects of EBID enabled MWNT interconnect fabrication.

Nanofabrication Process Design via EBID Simulations

For process design, we used a comprehensive dynamic model of EBID of residual hydrocarbon coupling mass transport, electron transport and scattering, and species decomposition to predict the deposition of carbon nanopillars on bulk substrates which we developed as an outcome of our fundamental work on EBID (see earlier in this report). The simulations predict the local species and electron density distributions, as well as the 3-D morphology and the growth rate of the deposit. Transport, scattering, and absorption of primary electron as well as secondary electron generation are treated using the Monte Carlo method. Low energy secondary electrons as well as high-energy backscattered electrons contribute to hydrocarbon decomposition due to their energy range matching peak dissociation and ionization reaction cross section energies for precursor molecules. The model was validated in follow up work [68] where the transient formation of hybrid, topologically complex microring-nanopilar deposits was investigated via combination of detailed simulations and EBID experiments (Figure 8). In particular, we demonstrated that the key input parameters for simulations, namely the surface diffusion coefficient (D_s) and initial surface concentration of the adsorbed species (C_0) can be estimated from two deposition experiments (e.g., at two different times of the same deposition sequence).

MWNT Interconnect Processing

Metal electrode fabrication

The 100 nm thick chromium electrodes on top of a 2 μm insulating silicon oxide layer were fabricated on a silicon wafer using standard photolithography techniques [69]. Several other groups [66,67,70,71] have taken a similar approach with metal electrode material varying from platinum [48] to aluminum [70]. The electrodes were designed so both the fixed [67] and floating point dielectrophoretic (DEP) [71] alignment experiments were possible. Seven devices with twelve possible interconnect sites each and varied electrode width and spacing were fabricated on each wafer.

MWNT selection

To ensure high quality of the MWNT, samples from six different companies were procured and compared. Specifically, the MWNT samples with varied averaged diameters and lengths from Cheap Tubes Inc. [72], Catalytic Materials [73], Nanostructured and Amorphous Materials [74], SES Research [75], Nanolab [76], and Helix Materials [77] companies were investigated. The MWNT samples were evaluated based on micro-Raman analysis and SEM visual inspection. The G (at ~1589 cm^{-1}[78]) to D (at ~1321-1341 cm^{-1} [78]) band Raman intensity ratio of the MWNT sample is a good indicator of the number of structural defects present [79]. The MWNT with diameters of 100-150 nm from Cheap Tubes Inc were found to have the highest G/D band ratio, and also the best quality from the SEM inspection. The Raman spectra and SEM images of the selected MWNT are shown in Figure 14a.

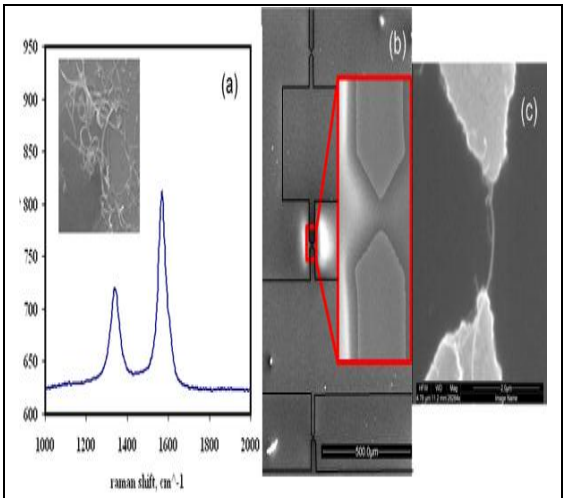

Fig. 14. (a) Raman Spectra of the selected MWNT [72] (insert on the right shows the corresponding SEM image), (b) Close up and full design of the DEP electrodes, (c) Example of DEP aligned MWNT from our experiment.

MWNT powder dispersion

Several different methods of MWNT powder dispersion were tested. Best results were obtained by placing a trace amount of MWNT powder in ethanol [70] or 1% Sodium Dodecyl Sulface (SDS)-deionized water (DI) mixture [71] and ultrasonicating the solution for a period of 15-25 minutes. The ethanol dispersed MWNT were difficult to work with because the solution wet the surfaces of the electrodes and evaporated too quickly for the DEP alignment to work.

Dielectrophoretic MWNT alignment

The procedure for DEP CNT alignment [66] consists of placing a small droplet of the MWNT solution in a region containing electrodes and applying DC, AC, or DC-AC potential for a short period of time on one "active" electrode, while grounding the second electrode and allowing the third electrode's potential to float [80]. If the strength of the non-uniform interelectrode electric field is sufficiently controlled to overcome Brownian motion [66], the CNT align themselves between the "active " and "floating" electrodes [71]. Song et al.[66] and Subramanian et al. [67] found the DEP alignment process to be sensitive to the electrode gap, applied voltage, MWNT solution concentration, droplet size, and duration of the process. The DEP procedure utilized consisted of the following steps:

- Fine needle placement of 1-2 μL droplet of the MWNT-1% SDS(surfactant)-DI solution in a region containing several chromium electrodes (solution MWNT concentration: 1-10 μg/mL, electrode spacing: 2-10 μm)
- Application of AC potential with a frequency of 5 MHz and peak-to-peak voltage of 10-20 V for a period of 1 minute
- Blowing off of the droplet to avoid additional tube deposition [67]
- Soaking wafer in DI water for a period of 15-20 minutes to eliminate residual SDS molecules [71].

As shown in Figure 14c, some of the tubes become aligned and form a connection between the electrodes.

MWNT end opening

The fact that most of MWNTs are capped at the ends [81] prevents establishment of electrical connection with the inner shells of the tube. Annealing [81,82], chemical etching [83,84], high energy electron beam [85], water assisted electron beam etching [86] and focused ion beam (FIB) [87] cutting are popular methods of MWNT cutting and end opening. Chemical etches indiscriminately damage all high curvature regions of CNTs and are difficult to control [83]. MWNT powder annealing experiments at temperatures of 550˚C were performed. Annealing at a higher temperature, even for short periods of time, resulted in complete destruction of the tubes. Annealing resulted in rather sporadic opening and cutting of the tubes. Since a cut at a specific point of the MWNT is desired, FIB will be utilized in the future experiments.

MWNT-Metal Interconnect Diagnostics

In-situ monitoring of EBID-enabled MWNT interconnect resistance

As shown in Figure 15a, our laboratory FEI Quanta 200 ESEM was modified so that a DC voltage can be applied between electrodes and the resulting current can be measured using Keithley 6485 Picoammeter. The system was successfully operated during EBID of carbon interface between a MWNT and metal electrode and. The obtained results, shown in Figure 15b compare well to those of Ando et al. [62], Madsen et al. [63], Yoshikawa et al. [88] and Kahng et al. [89].

Insulating to conductive a-C transition

Figure 15b shows a typical current vs. time measurement for EBID a-C MWNT-conductor interface formation. In this case EBID was performed at an accelerating voltage of 25 keV, spot size 3, high vacuum conditions (~10^{-6} Torr) and fixed

electrode bias of ~1.5 V. Focusing the electron beam on a small area surrounding the ends of the MWNT for 10-20 minutes gradually increased the measured current (corresponding to gradual decrease in the contact resistance due to build-up of a carbon deposit) until a drastic change was observed. According to Banhart et al. [90], Yoshikawa et al. [88], and Kahng et al. [89] this change can be attributed to the joule heating induced partial or full graphitization of the deposited a-C. To ensure that the MWNT did not contribute to the observed current jump, insulating to conductive transition in EBID made a-C lines connecting two electrodes was also induced. Figure 15b shows the prior to and post transition I-V curves for a ~100 nm thin 1 μm by 2 μm a-C line connecting two metal electrodes. Accurate measurement of the post-transition resistance of the film was difficult because the deposited films degraded and broke due to a significant joule heating.

.

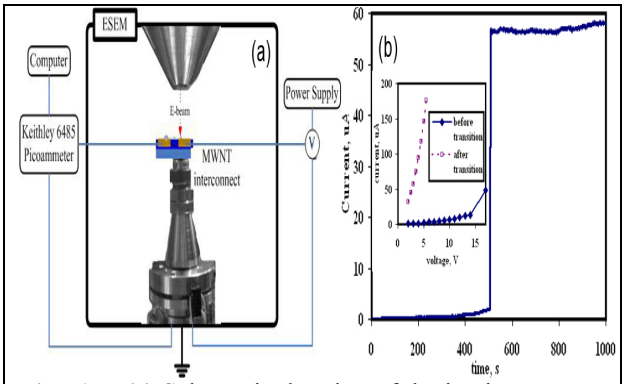

Fig. 15. (a) Schematic drawing of the in-situ current monitoring system, (b) Typical current vs. time measurement of EBID a-C MWNT-electrode interface. Insert shows the before and after insulating-to-conductive transition characteristics of an a-C film.

Conclusions and Future Work

We have demonstrated that EBID can be used for establishing Ohmic contact to multiple conducting shells of multiwall carbon nanotubes (MWNT), thus opening intriguing opportunities for using EBID in next generation nanoelectronic circuits. Basic understanding of the electron beam CNT interactions are of critical importance to developing a robust manufacturing process, and it is a subject of an on-going investigation. An additional focus of our on-going and future research on the improvement of resolution and deposition rate for the EBID process by modification of nozzle injection of precursor gas. It is conjectured that a greater hydrodynamic focusing of the precursor gas may improve the achievable deposition resolution, and a greater molecular velocity impinging on the surface may improve deposition rate. Concurrently with Gas-Jet-EBID experiments, we plan to develop and implement a methodology for simulation of the gas jet flow and to improve the construction of injection nozzles. The gas flow simulations should reveal the density and velocity of the gas impinging upon the surface as functions of temperature, pressure, incident angle, mixture ratio, and component mass ratio. In combination with electron transport simulations, this should allow us to develop an integrated modeling framework for multiscale simulations of Gas-Jet EBID, which will be validated by comparison with carefully designed EBID experiments using different precursors.

3. References

1. D.C. Beaulieu (2005) “Electron Beam Chemical Vapor Deposition of Platinum and Carbon”, M.S. Thesis, Woodruff School of Mechanical Engineering, Georgia Institute of Technology, Atlanta, GA.
2. Beaulieu, Yong Ding, Z.L. Wang, and W.J.Lackey “Influence of process variables on electron beam chemical vapor deposition of [platinum,” *J. Vac. Sci. and Tech. B*, **23**(5): p. 2151-2159. September 2005.
3. C. D. Lane, et al. (2005) "Electron stimulated desorption of cations from $SiCl_4$ multilayers adsorbed on Si(111)." *Surface Science* **593**:173-179.
4. C. D. Lane and T. M. Orlando,"State-resolved detection of neutral products produced during low-energy electron interactions with $SiCl_4$ multilayers", *J. Chem. Phys.*
5. Randolph, S. J. et al. Critical Reviews Solid State Materials Sciences, 2006. **31**: p. 55–89.
6. Ooi, T., et al. 2000. Miyazaki, Japan: IEEE.
7. Boggild, P., et al. Nanotechnology, 2001. **12**(3): p. 331-5.
8. Kohlmann-von Platen, K.T., et al. J. Vac. Sci. Technol. B, 1992. **10**(6): p. 2690-4.
9. Akama, Y., et al. Journal Vacuum Science Technology A, 1990. **8**(1): p. 429-33.
10. Silvis-Cividjian, N., et al. Microelectronic Engineering, 2002. **61-62**: p. 693-9.
11. Bret, T., et al. Applied Physics Letters, 2003. **83**(19): p. 4005-7.
12. Mitsuishi, K., et al. Ultramicroscopy, 2005. **103**(1): p. 17-22.
13. White, W.B., et al. Physical Review Letters, 2006. **97**(086101).
14. Silvis-Cividjian, N., *PhD Thesis*. 2002, University of Delft: Netherlands.

15. Fowlkes, J.D., et al. Journal Vacuum Science Technology B, 2005. **23**(6): p. 2825-2832.
16. Amman, M., et al. Journal of Vacuum Science & Technology B, 1995. **14**(1): p. 54-62.
17. Ueda, K. and M. Yoshimura. Thin Solid Films, 2004(464-465): p. 331-334.
18. Muller, K., Optik, 1971. **33**: p. 296.
19. Reimer, L. and M. Wachter, Ultramicroscopy, 1978. **3**: p. 169-174.
20. Rykaczewski, K., et al. Journal of Applied Physics, 2007. **101**(5).
21. Taylor, P.A., et al. Journal of American Chemical Society, 1992. **114**: p. 6754-6760.
22. Joy, D.C., *Monte Carlo Modeling for Electron Microscopy and Microanalysis*. 1995, New York, London: Oxford University Press.
23. Wong, B.T., et al. Journal of Heat Transfer, 2004. **126**(4): p. 566-576.
24. Randolph, S.J., et al. Journal of Applied Physics, 2005. **97**(12): p. 124312.
25. Dapor, M., *Electron-beam interactions with solids : application of the Monte Carlo method to electron scattering problems*. 2003, New York: Springer.
26. Zhang, Z., *Nano/microscale Heat Transfer*. 2007: McGraw-Hill.
27. Ziman, J.M., *Electrons and phonons; the theory of transport phenomena in solids*. The International series of monographs on physics. 1960, Oxford: Clarendon Press.
28. Vas'ko, F.T. and O.E. Raichev, *Quantum kinetic theory and applications : electrons, photons, phonons*. 2005, New York: Springer.
29. Utke, I., et al. Microelectronic Engineering, 2004. **73-74**: p. 553-8.
30. Utke, I., et al. Advanced Engineering Materials, 2005. **7**(5): p. 323-331.
31. Pop, E., S. et al. Proceedings of 2002 ASME IMECE. 2002. New Orleans, LO, USA.
32. Bullen, A.J., et al. Journal of Applied Physics, 2000. **88**(11): p. 6317-6320.
33. Bhattacharyya, S. and S.R.P. Silva, Thin Solid Films, 2005. **482**(1-2): p. 94-98.
34. Bezryadin, A. and C. Dekker. Journal Vacuum Science Technology B, 1997. **15**(4): p. 793-799.
35. Davies, S.T. and B. Khamsehpour. Vacuum, 1996. **47**(5): p. 455-62.
36. Gortz, W., B. et al. Journal Vacuum Science Technology B, 1995. **13**(1): p. 34-39.
37. Okada, S., et al. Japanese Journal of Applied Physics Part 1, 2005. **44**(7B): p. 5646-5650.
38. Fujita, J., et al.. Journal Vacuum Science Technology B, 2003. **21**(6): p. 2990-2993.
39. Uesugi, K. and T. Yao. Ultramicroscopy, 1992. **42**: p. 1443-1445.
40. Rykaczewski, K., et al., *Dynamic growth of carbon nanopillars and microrings in electron beam induced dissociation of residual hydrocarbons.* Ultramicroscopy, 2008.
41. Rykaczewski, K., W. White, and A. Fedorov, *Analysis of electron beam induced deposition (EBID) of residual hydrocarbons in electron microscopy.* Journal of Applied Physics, 2007. **101**: p. 054307.
42. Browning, R., et al., *Empirical forms for the electron/atom elastic scattering cross sections from 0.1 to 30 keV.* Journal of Applied Physics, 1994. **76**: p. 2016.
43. Fowlkes, J.D., S.J. Randolph, and P.D. Rack. *Growth and simulation of high-aspect ratio nanopillars by primary and secondary electron-induced deposition*. 2005: AVS.
44. Alman, D.A., D.N. Ruzic, and J.N. Brooks, *A hydrocarbon reaction model for low temperature hydrogen plasmas and an application to the Joint European Torus.* Physics of Plasmas, 2000. **7**(5): p. 1421-1432.
45. Kwitnewski, S., E. Ptasinska-Denga, and C. Szmytkowski, *Relationship between electron-scattering grand total and ionization total cross sections.* Radiation Physics and Chemistry, 2003. **68**(1-2): p. 169-174.
46. Moskalenko, A., et al., *Electron-beam-induced welding of 3D nano-objects from beneath.* NANOTECHNOLOGY, 2007. **18**(2): p. 25304.
47. *International Technology Roadmap for Semiconductors.* http://public.itrs.net.
48. Dong, L.F., et al., *Effects of local Joule heating on the reduction of contact resistance between carbon nanotubes and metal electrodes.* Journal of Applied Physics, 2007. **101**(2).
49. Anantram, M.P. and F. Leonard, *Physics of carbon nanotube electronic devices.* Reports on Progress in Physics, 2006. **69**(3): p. 507-561.
50. Graham, A.P., et al., *How do carbon nanotubes fit into the semiconductor roadmap?* Applied Physics a-Materials Science & Processing, 2005. **80**(6): p. 1141-1151.
51. Tersoff, J., *Contact resistance of carbon nanotubes.* Applied Physics Letters, 1999. **74**(15): p. 2122-2124.
52. Frank, S., et al., *Carbon nanotube quantum resistors.* Science, 1998. **280**(5370): p. 1744-1746.
53. Nihei, M., et al. *Low-resistance multi-walled carbon nanotube vias with parallel channel conduction of inner shells*. 2005. Burlingame, CA, United States: Institute of Electrical and Electronics Engineers Computer Society, Piscataway, NJ 08855-1331, United States.
54. Sato, S., et al. *Novel approach to fabricating carbon nanotube via interconnects using size-*

controlled catalyst nanoparticles. 2006. Burlingame, CA, USA: IEEE.
55. Li, H.J., et al., *Multichannel ballistic transport in multiwall carbon nanotubes.* Physical Review Letters, 2005. **95**(8).
56. Langford, R.M., et al., *Comparison of different methods to contact to nanowires.* Journal of Vacuum Science & Technology B, 2006. **24**(5): p. 2306-2311.
57. Dockendorf, C.P.R., et al., *Individual carbon nanotube soldering with gold nanoink deposition.* Applied Physics Letters, 2007. **90**(19).
58. Bachtold, A., et al., *Contacting carbon nanotubes selectively with low-ohmic contacts for four-probe electric measurements.* Applied Physics Letters, 1998. **73**(2): p. 274-276.
59. Rice, P., et al., *Broadband electrical characterization of multiwalled carbon nanotubes and contacts*. Nano Letters, 2007. **7**(4): p. 1086-1090.
60. Bussolotti, F., et al., *In situ manipulation and electrical characterization of multiwalled carbon nanotubes by using nanomanipulators under scanning electron microscopy.* Physical Review B, 2007. **76**(12).
61. Fedorov, A.G., K. Rykaczewski, and W.B. White, *Transport issues in focused electron beam chemical vapor deposition.* Surface & Coatings Technology, 2007. **201**(22-23): p. 8808-8812.
62. Ando, A., et al., *Improvement of electrical contact at carbon nanotube/Pt by selective electron irradiation.* Physica E-Low-Dimensional Systems & Nanostructures, 2004. **24**(1-2): p. 6-9.
63. Madsen, D.N., et al., *Soldering of nanotubes onto microelectrodes.* Nano Letters, 2003. **3**(1): p. 47-49.
64. Molhave, K., et al., *Constructing, connecting and soldering nanostructures by environmental electron nsing of doubly clamped multi-walled carbon nanotubes.* Nanotechnology, 2008. **19**(1): p. 4.
65. Molhave, K., et al., *Solid gold nanostructures fabricated by electron beam deposition.* Nano Letters, 2003. **3**(11): p. 1499-503.
66. Song, J.W., et al., *Characterization and air pressure secarbon nanotube FETs by Kelvin probe force microscopy.* Japanese Journal of Applied Physics Part 1-Regular Papers Short Notes & Review Papers, 2005. **44**(4A): p. 1633-1636.
67. Subramanian, A., et al. *Micro and Nanorobotic Assembly Using Dielectrophoresis*. in *Robotics: Science and Systems I*. 2005. Massachusetts Institute of Technology, Cambridge, Massachusetts.
68. Rykaczewski, K., et al., *Dynamic growth of carbon nanopillars and microrings in electron beam induced dissociation of residual hydrocarbons.* Ultramicroscopy, 2008. **108**(9): p. 989-92.
69. Miyato, Y., et al., *Local surface potential measurements of beam deposition.* Nanotechnology, 2004. **15**(8): p. 1047-1053.
70. Close, G.F., et al., *A 1GHz Integrated Circuit with Carbon Nanotube Interconnects and Silicon Transistors.* Nano Letters, 2008. **8**(2): p. 706-709.
71. Dong, L.F., et al., *Floating-potential dielectrophoresis-controlled fabrication of single-carbon-nanotube transistors and their electrical properties.* Journal of Physical Chemistry B, 2005. **109**(27): p. 13148-13153.
72. www.cheaptubesinc.com
73. www.catalyticmaterials.com.
74. www.nanoamor.com.
75. www.sesres.com.
76. www.nano-lab.com.
77. www.helixmaterial.com.
78. Qian, W.Z., et al., *Quantitative Raman characterization of the mixed samples of the single and multi-wall carbon nanotubes. Carbon, 2003. **41**(9):p.1851-1854.*
79. Costa, S., et al., Characterization of carbon nanotubes by Raman spectroscopy. Materials Science-Poland, 2008. 26(2): p. 433-441.
80. Subramanian, A., et al., Local control of electric current driven shell etching of multiwalled carbon nanotubes. Applied Physics a-Materials Science & Processing, 2007. 89(1): p. 133-139.
81. Ajayan, P.M., et al., Opening Carbon Nanotubes with Oxygen and Implications for Filling. Nature, 1993. 362(6420): p. 522-525.
82. Ajayan, P.M. and S. Iijima, Capillarity-Induced Filling of Carbon Nanotubes. Nature, 1993. 361(6410): p. 333-334.
83. Tsang, S.C., et al., A Simple Chemical Method of Opening and Filling Carbon Nanotubes. Nature, 1994. 372(6502): p. 159-162..cheaptubesinc.com
84. Ito, T., L. Sun, and R.M. Crooks, *Electrochemical etching of individual multiwall carbon nanotubes.* Electrochemical and Solid State Letters, 2003. **6**(1): p. C4-C7.
85. Banhart, F., *Irradiation effects in carbon nanostructures.* Reports on Progress in Physics, 1999. **62**(8): p. 1181-1221.
86. Yuzvinsky, T.D., et al., *Precision cutting of nanotubes with a low-energy electron beam.* Applied Physics Letters, 2005. **86**(5): p. 3.
87. Lan, C., D.N. Zakharov, and R.G. Reifenberger, *Determining the optimal contact length for a metal/multiwalled carbon nanotube interconnect.* Applied Physics Letters, 2008. **92**(21): p. 3.
88. Yoshikawa, Y., S. Akita, and Y. Nakayama, *Barrier modification at contacts between carbon nanotube and Pt electrode using well-controlled Joule heating.* Japanese Journal of Applied Physics Part 2-Letters & Express Letters, 2007. **46**(12-16): p. L359-L361.
89. Kahng, Y.H., et al., *The role of an amorphous carbon layer on a multi-wall carbon nanotube*

attached atomic force microscope tip in making good electrical contact to a gold electrode. Nanotechnology, 2008. **19**(19): p. 7.
90. Banhart, F., *The formation of a connection between carbon nanotubes in an electron beam.* Nano Letters, 2001. **1**(6): p. 329-332.
91. Eres, G., *Application of supersonic molecular jets in semiconductor thin film growth.* Critical Reviews in Solid State and Materials Sciences, 1998. **23**(4): p. 275-322.